Bachelor Thesis

The Quiet Sun as a Background Source for Compton Spectrometer and Imager

Linus Stricker

Würzburg, August 2024

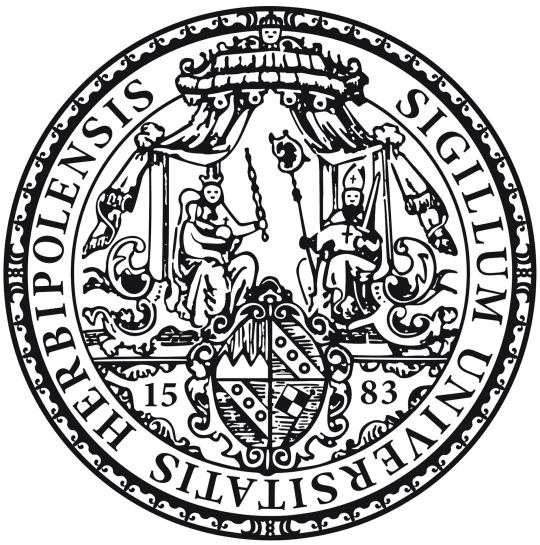

Julius-Maximilians-Universität Würzburg
Faculty of Physics and Astronomy

Supervisor: Dr. Thomas Siegert

Abstract

Context: The Sun in its quiescent state is expected to be a persistent source of gamma-rays. The possible emission of a 511 keV line flux from quiet stars could contribute to the Galactic 511 keV emission and help to explain the measured distribution.
Aims: The goal of this thesis is to create possible models of the quiescent solar gamma-ray flux and to estimate how significant they would be measured by the Compton Spectrometer and Imager (*COSI*). This will allow an estimate of the Galactic 511 keV emission from main sequence stars in their quiescent state.
Methods: A power-law model and a gaussian model for the 511 keV emission is fitted to upper limits of the quiet Sun's gamma-ray flux from 100 keV to 10 MeV. This results in different models, which are constrained and weighted with a likelihood. The significance of these model fluxes compared to *COSI*'s instrumental background and the galactic background, is estimated using a signal to noise ratio approximation. The Sun is treated as a stationary source for a day for *COSI* and then moved by $\sim 1^{\circ}$. This approach is used to determine the resulting significance that accumulates over the 2 yr mission period. An astrophysical model from Peterson et al. (1966) for the quiet solar flux is also tested.
Results: A maximum significance was found at two positions: $(\ell, b) = (-87^{\circ}, 60^{\circ})$ and $(\ell, b) = (94^{\circ}, -60^{\circ})$. A 511 keV line flux of $\sim 5.5 \times 10^{-6}\,\mathrm{photons\,s^{-1}\,cm^{-2}}$ has a significance of 3σ within 2 yr. About 24% of the sky would have a higher significance than the Sun if there were a Sun-like stationary source with the same flux between 150–5000 keV. The astrophysical model of the gamma-ray continuous flux from the quiet Sun from Peterson et al. (1966) with a flux of $4.68 \times 10^{-5}\,\mathrm{photons\,s^{-1}\,cm^{-2}}$, resulted in a significance of $\sim 1\sigma$ for the 2 yr observation time.
Conclusions: The Sun might be a varying source for *COSI* in terms of continuum and 511 keV emission, but the Galactic 511 keV emission is probably unaffected by the contribution of main sequence stars.

Zusammenfassung

Kontext: Es wird erwartet, dass die Sonne in ihrem ruhigen Zustand eine kontinuierliche Quelle von Gammastrahlen ist. Die mögliche Emission einer 511 keV Linie von ruhigen Sternen könnte zur Galaktischen 511 keV-Emission beitragen und helfen, die gemessene Verteilung zu erklären.
Ziel: Das Ziel dieser Arbeit ist es, mögliche Modelle des ruhigen solaren Gammastrahlenflusses zu erstellen und abzuschätzen, wie signifikant diese vom Compton Spectrometer and Imager (*COSI*) gemessen werden könnten. Dies ermöglicht es, die Galaktische 511 keV-Emission von Hauptreihensternen in ihrem ruhigen Zustand abzuschätzen.
Methoden: Ein Potenzgesetzmodell und ein Gaußmodell für die 511 keV-Emission werden an upper limits des ruhigen solaren Gammastrahlenflusses von 100 keV bis 10 MeV angepasst. Dies führt zu verschiedenen Modellen, die eingeschränkt und mit einer Likelihood gewichtet werden. Die Signifikanz dieser Modellflüsse im Vergleich zu *COSI*'s instrumentalem Hintergrundstrahlung und dem Galaktischen Hintergrundstrahlung wird mit dem signal to noise Verhältnis abgeschätzt. Die Sonne wird für einen Tag als stationäre Quelle für *COSI* behandelt und dann um etwa $\sim 1^\circ$ verschoben. Mit diesem Ansatz wird die resultierende Signifikanz bestimmt, die sich über den Zeitraum von 2 yr Missionsdauer aufbaut. Ein astrophysikalisches Modell von Peterson et al. (1966) für den ruhigen solaren Fluss wird ebenfalls getestet.
Ergebnisse: Eine maximale Signifikanz wurde an zwei Positionen gefunden: $(\ell, b) = (-87^\circ, 60^\circ)$ und $(\ell, b) = (94^\circ, -60^\circ)$. Ein 511 keV-Linienfluss von etwa $5,5 \times 10^{-6}$ photons $\mathrm{s}^{-1}\,\mathrm{cm}^{-2}$ zeigt innerhalb von 2 Jahren eine Signifikanz von 3σ. Etwa 24% des Himmels würde eine höhere Signifikanz als die Sonne aufweisen, wenn dort eine stationäre Quelle mit einem Fluss zwischen 150–5000 keV ähnlich der Sonne vorhanden wäre. Das astrophysikalische Modell des kontinuierlichen Gammastrahlenflusses der ruhigen Sonne von Peterson et al. (1966) mit einem Fluss von $4,68 \times 10^{-5}$ photons $\mathrm{s}^{-1}\,\mathrm{cm}^{-2}$ ergab für die 2 yr Beobachtungszeit eine Signifikanz von $\sim 1\sigma$.
Schlussfolgerung: Die Sonne könnte für *COSI* eine variable Quelle in Bezug auf kontinuierliche und 511 keV-Emission sein, aber die galaktische 511 keV-Emission wird wahrscheinlich nicht durch den Beitrag von Hauptreihensternen beeinflusst.

Contents

1. Introduction

Measuring X-ray and gamma-ray emissions from astrophysical sources provides insight into highly energetic processes in the Universe. However, the energy range from about 100 keV to 50 MeV remains the least observed region of the entire electromagnetic spectrum. To shed light on a region in this so-called 'MeV gap", the Compton Spectrometer and Imager (*COSI*) Small Explorer (*SMEX*) mission is scheduled to launch in 2027, and will operate in the 0.2–5 MeV range (Tomsick et al., 2019). One potential source that could be measured for the first time in this band during this mission is the quiet Sun. While the Sun emits significant amounts of gamma radiation during its flares, it is also expected to be a persistent source of gamma-rays in its quiescent state. COSI will have the sensitivity and capability to constrain the emission of the Sun along the ecliptic in addition to the many other astrophysical sources. Since this quiet solar gamma-ray flux in this range has not been observed yet, its detection would provide an opportunity to validate existing models that describe this emissions a combination of inverse compton scattering, interaction of cosmic rays with the solar atmosphere, and reflected cosmic X-rays. Additionally, distinguishing the Sun from the remaining sources is important to minimise unwanted artefacts in image reconstruction and spectral fits.

Another important reason why the spectrum of the quiet Sun is of great interest is the possible detection of the 511 keV line associated with positron annihilation. The so-called 'positron puzzle" remains an unresolved conundrum. It concerns the unexplained shape of the 511 keV map of the Galaxy. Fig. 1.1 shows the bright bulge emission outshining the thick disc emission of the 511 keV flux (Siegert, 2023). No other map at different wavelengths shows similarities to this distribution (Fig. 1.1). The only maps that produces adequate figure of merits when comparing to the 511 keV from INTEGRAL/SPI are the infrared red from 1.25 to 4.9 micron (IR in Fig. 1.1). Since stars contribute significantly to this IR emission, they could be a potential source of the 511 keV disc emission. The 511 keV line has been detected in X-class solar flares. Through particle acceleration and the subsequent decay of pions, positrons are produced, which mainly contribute to this emission. Flaring stars are thus already an established source of 511 keV emission. Therefore, studying the 511 keV flux from the quiet Sun will help to investigate this hypothesis.

In this work I will develop different models of the quiescent solar gamma-ray emission based on previous measurements from 100 keV to 10 MeV. These models will then be

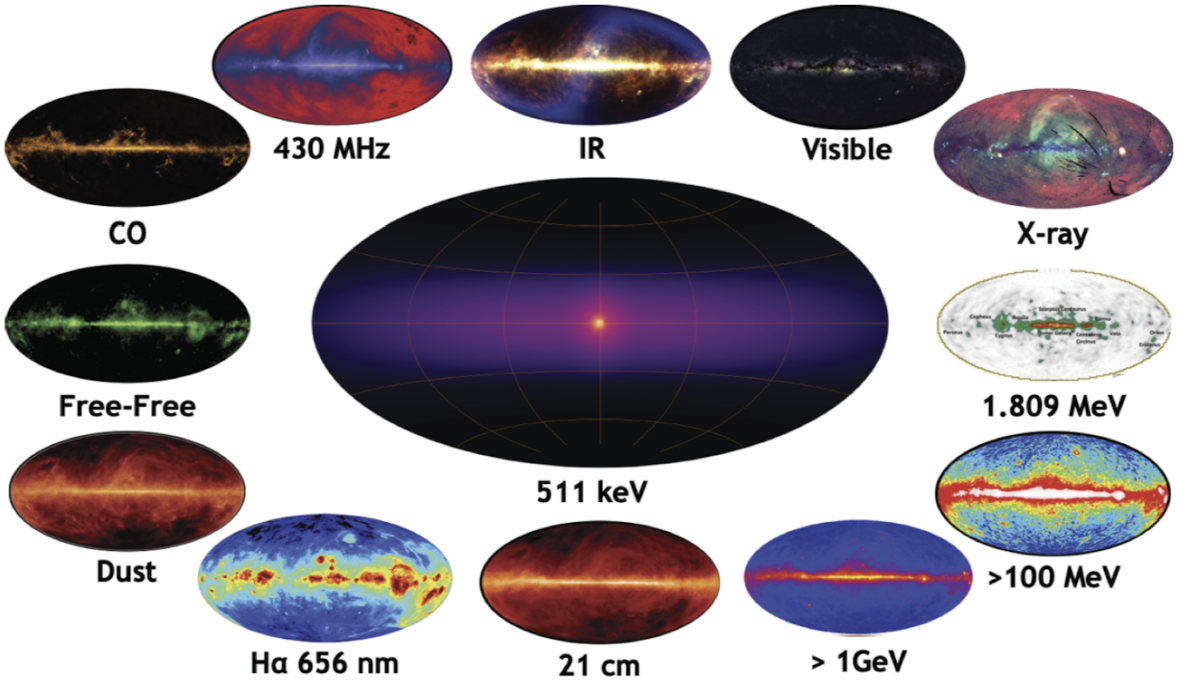

Figure 1.1.: Measured full-sky maps at different wavelengths and due to different emission processes. Figure taken from (Siegert, 2023).

tested to estimate their significance as measured by *COSI*. For this, an approximation of the signal-to-noise ratio is used. The ratio is calculated by comparing the estimated counts from different models to the square root of the total detected counts from the sky, which include the instrumental background, the Milky Way gamma-ray emission, and the counts from the model itself.

This thesis is organised as follows: Chapter 2 describes the physical processes leading to the solar gamma-ray emission and presents previous measurements of the quiet solar emission. Chapter 3 introduces Bayesian fitting methods and the fitting of the models is carried out. Chapter 4 explains the COSI mission concept and Chapter 5 assesses the significance of various models. In Chapter 6 the simulation of a physical model for the *COSI* instrument is conducted.

2. The Spectrum of the Quiet Sun

2.1. Solar Structure

The internal structure of the Sun determines the intensities of the emission mechanisms: With a mass of $M_\odot \approx 2 \times 10^{30}\,\mathrm{kg}$ and an absolute brightness of $M = +4.83\,\mathrm{mag}$, the Sun is located on the main sequence of the Hertzsprung-Russell diagram and is classified as a yellow dwarf of spectral class type G2V. As shown in Fig. 2.1, the Sun can be considered as build up of different radial regions. The inner zones consist of the core, the radiative zone, and the convective zone. The Sun's radius is $R_\odot \approx 696 \times 10^3\,\mathrm{km}$ and the core extends up to $0.27\,R_\odot$. It serves as the energy source of the Sun, where nuclear fusion occurs mainly through the proton-proton (pp) chain. This chain, converting hydrogen (H) into helium (He), generates 98% of the Sun's luminosity. Although the core makes up only about 1.5% of the Sun's volume, it contains half of its mass. The temperature at the innermost part of the core is about 15 MK, with a density of $150\,\mathrm{g\,cm^{-3}}$. At the outer edge of the core, the temperature drops to around 7 MK, and the density decreases to $20\,\mathrm{g\,cm^{-3}}$ (Fig. 2.2). Given the energy production of the Sun is dominated by the pp-chain and sub-dominantly by the carbon-nitrogen-oxygen (CNO) cycle, its lifetime on the main sequence is about 10 Gyr.

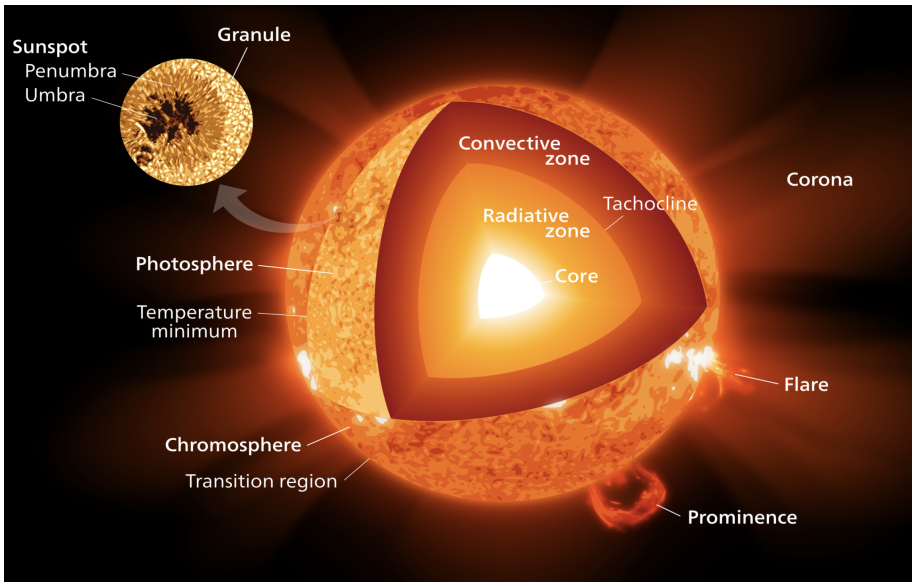

Figure 2.1.: Schematic section of the interior of the Sun. Figure taken from (Tie, 2015).

The next zones following the core are distinguished based on the energy transport that occurs within them. The region closest to the core is known as the radiative zone [Fig. 2.1], where energy transport occurs in the form of radiation. The reaction products of the pp chain thermalize in the core. Due to the temperature of the core, the thermal radiation primarily lies in the soft X-ray range. Since the photons constantly interact with particles and are redirected by them along their path through the radiative zone, through processes such as absorption or scattering, they undergo a random walk motion. As a result, photons require a time of 10,000 to 170,000 yr to reach the outer boundary of the radiative zone. As the emitted radiation power spreads over increasingly larger spherical surface areas, the temperature decreases with increasing radius. As shown in Fig. 2.2, the radiative zone is the broadest inner region of the Sun, with its outer boundary located at $0.7\,R_{\odot}$. Once the temperature has dropped to about 2 MK, the convective zone begins (Fig. 2.2). At this temperature, the heavier atomic nuclei in this layer are capable of capturing electrons. Consequently, the opacity of these layers increases, making it more difficult for radiation to penetrate them (Hathaway, 2022). Heat accumulates in the inner layer of the convective zone, leading to a sharp increase in the temperature gradient dT/dr. Once the temperature gradient exceeds the adiabatic gradient, energy transport occurs in the form of convection. The adiabatic gradient indicates how the temperature of the plasma would change if it were moved radially outward into higher layers without any heat exchange occurring (Hathaway, 2022). Large cells of rising matter form, expanding

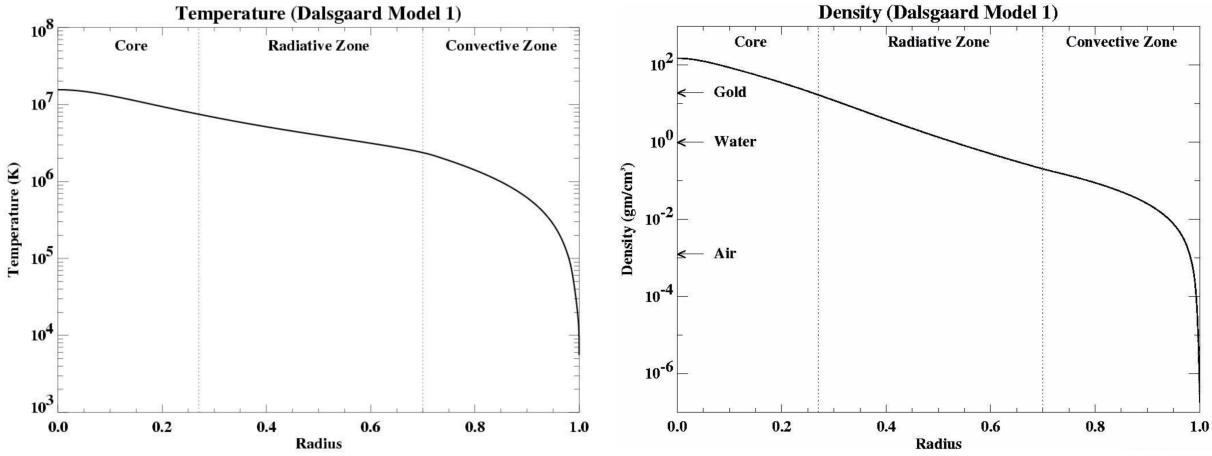

Figure 2.2.: The temperature (left) and density (right) within the Sun as a function of radius. Figure taken from (Hathaway, 2022).

and cooling as they ascend. Through this process, energy is predominantly carried to the surface, where the temperature eventually reaches a value of about 5,700 K (Hathaway, 2022). Those cells are visible on the solar surface as granules and supergranules (Fig. 2.1). The granulation pattern is constantly changing as new cells rise and old ones descend. The transitional region between the radiative and convective zones is known as the Tachocline. The convective motion of matter decreases in this thin layer until it

completely ceases at its inner edge. Due to the significant change in the flow velocity of matter/plasma in this zone, it is assumed that the Sun's magnetic field is generated in here (Hathaway, 2022).
At a certain altitude, the density has decreased so much that the mean free path of photons has become large enough for most of them to escape. This boundary defines photosphere. This is the visible surface of the Sun and emits the majority of solar radiation. In this region, features such as sunspots can be observed. These dark spots are caused by concentrated magnetic flux, which inhibits convection and therefore lowers the temperature. Energy transport within this layer primarily occurs through convection and radiation. Consequently, the temperature decreases outward until reaching a value of about 4,000 K (Morton et al., 2022). Beyond this point, the temperature begins to rise again into higher layers. This marks the beginning of the chromosphere which is a layer of the solar atmosphere. The ∼1500 km thick chromosphere is a non-homogeneous layer with highly dynamic behavior. The density of the chromosphere decreases from about $10^{-6}\,\mathrm{g\,cm^{-3}}$ to about $10^{-14}\,\mathrm{g\,cm^{-3}}$ at its outermost layer with temperatures reaching values up to 20,000 K (Hathaway, 2022). The chromosphere shows a web like pattern outlining the supergranuels in the photosphere. The fluid flow in the supergranuels transport magnetic field bundles towards the edge of the cells, creating this network (Hathaway, 2022). Long pillar like plasma eruptions, the so called spicules, pervade the whole chromosphere. They arise through interaction with the Sun's magnetic field and carry energy outward, which may explain the increasing temperature in the chromosphere (Krummheuer, 2019).
The outermost region of the solar atmosphere is the corona, which consists of an almost completely ionised plasma. It is much less dense ($\sim 10^{-17}\,\mathrm{g\,cm^{-3}}$) than the chromosphere, but is superheated to temperatures above 1 MK. (Hathaway, 2022). The corona shows a number of features such as streamers, plumes and loops. Between the chromosphere and the corona lies the transition region. It is a thin and highly irregular layer of the Sun's atmosphere. Heat from the corona flows into the chromosphere, creating this thin region where the temperature rapidly drops.

2.2. The Gamma-Ray Spectrum of the Quiet Sun

The radiation emitted by the Sun is primarily thermal radiation. Fig. 2.3 shows that the Sun can be considered an imperfect black body. Through Planck's radiation law,

$$P(\lambda, T)d\lambda = \frac{8\pi}{\lambda^5}\frac{hc}{e^{\frac{hc}{\lambda k_\mathrm{B} T}} - 1}d\lambda \tag{2.1}$$

where $h = 6.6261 \cdot 10^{-34}\,\mathrm{Js}$ is Planck's constant, $k_\mathrm{B} = 1.3806 \cdot 10^{-23}\,\mathrm{J\,K^{-1}}$ is Boltzmann's constant and $c = 2.9971 \cdot 10^{8}\,\mathrm{m\,s^{-1}}$ is the speed of light in vacuum, the solar spectrum can be approximated as a black body with an effective temperature of $T = 5777\,\mathrm{K}$. The

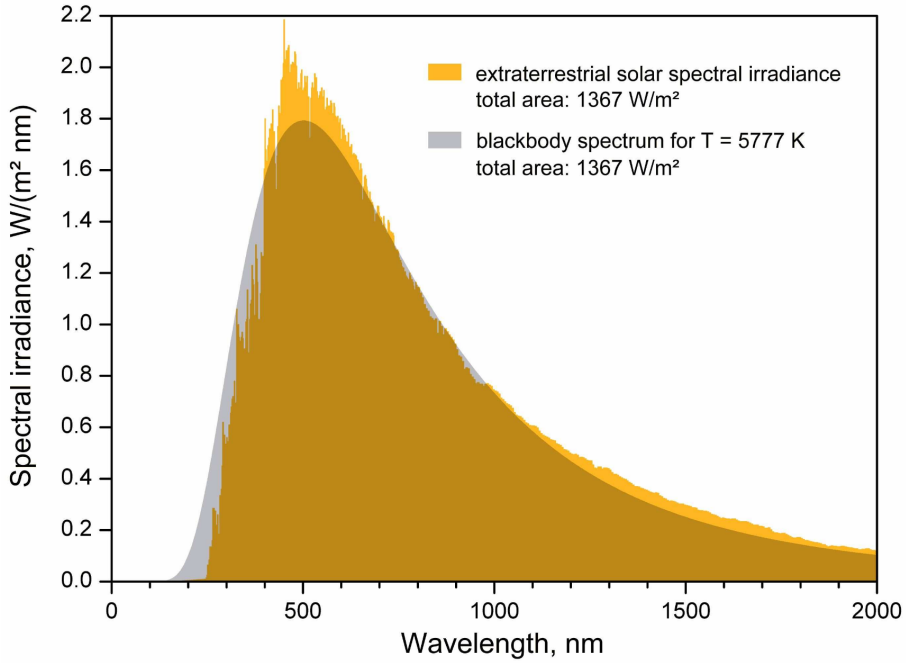

Figure 2.3.: The Sun's extraterrestrial irradiance compared to a blackbody spectrum at $T = 5777\,\mathrm{K}$. The total intensity of both spectra is $1367\,\mathrm{W\,m^{-2}}$ (Smerlack, 2010).

peak of the radiation lies in the range of green visible light, and the radiation mainly extends from the near ultraviolet ($\sim 200\,\mathrm{nm}$) to the far infrared ($\sim 25.000\,\mathrm{nm}$). Since the intensity of thermal radiation decreases exponentially for $h\frac{c}{\lambda} \gg k_\mathrm{B}T$, there is hardly any hard X-ray and gamma radiation present in the form of thermal radiation.
In its quiet state, the intrinsic high-energy radiation from the Sun is particularly weak, and only events such as flares, sunspots, or coronal mass ejections, produce strong gamma-ray emission. However, even in quiet regions, the solar atmosphere is filled with small-scale events like jets, minifilament eruptions, and so-called "nanoflares", which are considered to contribute to the gamma-ray spectrum of the quiet Sun (Hannah et al., 2007). The strongest contribution to the gamma-ray spectrum of the quiet Sun is expected from the interaction of cosmic rays with the solar atmosphere. gamma-rays, for example, are produced through interactions with the Sun's atmosphere, magnetic field, or photon field (Orlando et al., 2021). In the following, these processes will be described.

2.2.1. Inverse Compton Emission

Compton scattering is an interaction between a photon and an electron. In the classical frame, a photon collides with a stationary electron and scatters elastically with it. The photon transfers part of its energy to the electron, thereby changing its wavelength. As a

result, the energy of the photon changes to

$$E_{\gamma_f} = \frac{E_{\gamma_i}}{1 + \frac{E_{\gamma_i}}{m_e c^2}(1 - \cos\theta)}. \tag{2.2}$$

Here, $E_{\gamma f}$ is the photon energy after the scattering, $E_{\gamma i}$ is the photon energy before the collision and θ is the angle between the initial propagation direction of the photon and the propagation direction of the scattered photon, the so-called Compton scattering angle.
The inverse Compton (IC) effect can be seen as a reversed Compton scattering. Here, a moving electron scatters off a photon, scattering elastically and transferring some of its energy to the photon. Since it usually involves highly energetic electrons, this effect must be considered relativistically. When viewed from the rest frame of the electron, the ordinary Compton effect occurs. According to the relativistic Doppler effect, with the Lorentz factor $\gamma = 1/\sqrt{1-\beta^2}$, $\beta = v/c$ and the angle α between the direction of motion of the electron and the photon, the initial energy of the incident photon writes

$$E'_{\gamma_i} = E_{\gamma_i}\gamma(1 - \beta\cos\alpha). \tag{2.3}$$

This results in the energy of the scattered photon in the rest frame of the electron:

$$E'_{\gamma_f} = \frac{E'_{\gamma_i}}{1 + \frac{E'_{\gamma_i}}{m_e c^2}(1 - \cos\theta')}. \tag{2.4}$$

Transforming E'_{γ_f} back into the laboratory frame gives:

$$E_{\gamma_f} = E'_{\gamma_f}\gamma(1 - \beta\cos\alpha'). \tag{2.5}$$

Considering the case $E'\gamma_i \ll m_e c^2$ and a typical collision angle $\alpha \sim \alpha' \sim \frac{\pi}{2}$, (Eq. 2.5) can be approximated to

$$E_{\gamma_f} \sim \gamma^2 E_{\gamma_i}. \tag{2.6}$$

This shows that a thermal photon emitted in the visible range $E_{\gamma_f} \sim 1\,\mathrm{eV}$ can be converted into the MeV range through inverse Compton scattering by a cosmic-ray (CR) electron, when $\gamma = 10^3$. Thus, inverse Compton scattering is an effect that can convert the Sun's thermal radiation into gamma radiation.

Modulation of the IC Emission

The quiescent gamma-ray spectrum of the Sun can be divided into a point-like emission from the solar disc and an additional extended emission due to inverse Compton radiation.

In Abdo et al. (2011) the detected gamma-rays from the Sun were studied with the Large Area Telescope (LAT) on the Fermi spacecraft (Fermi-LAT). Fig. 2.4 shows the integral intensity for events with energies $\geq 500\,\mathrm{MeV}$ as a function of the angle of elongation. The extended emission and the solar disc emission at $\sim 0.5^\circ$ are clearly visible. Beyond an angle of elongation of $\sim 20^\circ$, the solar emission spectrum is indistinguishable from the background.

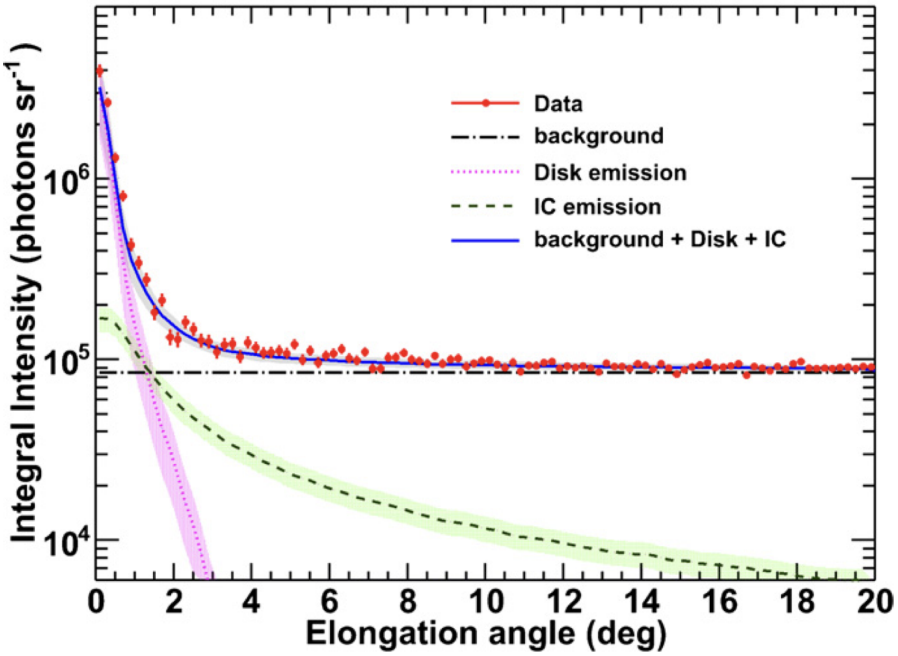

Figure 2.4.: Integral intensity of solar radiation $\geq 500\,\mathrm{MeV}$ as a function of the angle of elongation up to 20. The red points correspond to data from Fermi-LAT, the purple dotted line represents the fitted disc emission and the green dashed line represents the fitted extended IC emission. The background is the same for all elongation angles and is also derived from the Fermi-LAT data. The blue line represents the sum of the disc emission, the IC emission and the background. Figure taken from (Abdo et al., 2011).

The main components needed to calculate the IC emission are the cosmic ray electron spectrum and the solar radiation field. In Orlando et al. (2021), the electron spectrum was calculated using the force field approximation. Since the CR electron spectrum is influenced by the Sun, this modulation must be taken into account in the calculation, and the modulated differential intensity in the heliosphere $J(r, E_e)$ thus depends on the distance from the Sun:

$$J(r, E_e) = J(\infty, E_e + \Phi(r)) \frac{E_e(E_e + 2E_0)}{(E_e + \Phi(r) + 2E_0)(E_e + \Phi(r))} \tag{2.7}$$

Here $J(\infty, E_e + \Phi(r))$ is the local interstellar all-electron spectrum, E_0 is the rest energy of the electron, E_e is the kinetic energy of the particle, and $\Phi(r)$ is the modulation potential as a function of radius r. As the modulation potential for $r < 1\,\mathrm{AU}$ is quite uncertain, a

constant value of $\Phi(1\,\mathrm{AU}) = \Phi_0$ is used in this region. As the modulation increases closer to the Sun, causing the CR electron spectrum to become more attenuated, this approach leads to an upper bound estimate of the IC emission. Fig. 2.5 shows the all-electron spectra fitted to two different measurements of CR electrons by PAMELA and AMS-02 at 1 AU (Orlando et al., 2021). The PAMELA data were taken during a solar maximum period, while the AMS-02 data represent a solar minimum period. The modulation effect of the Sun on the CR electrons becomes negligible at energy levels above $\sim 10^4$ MeV.

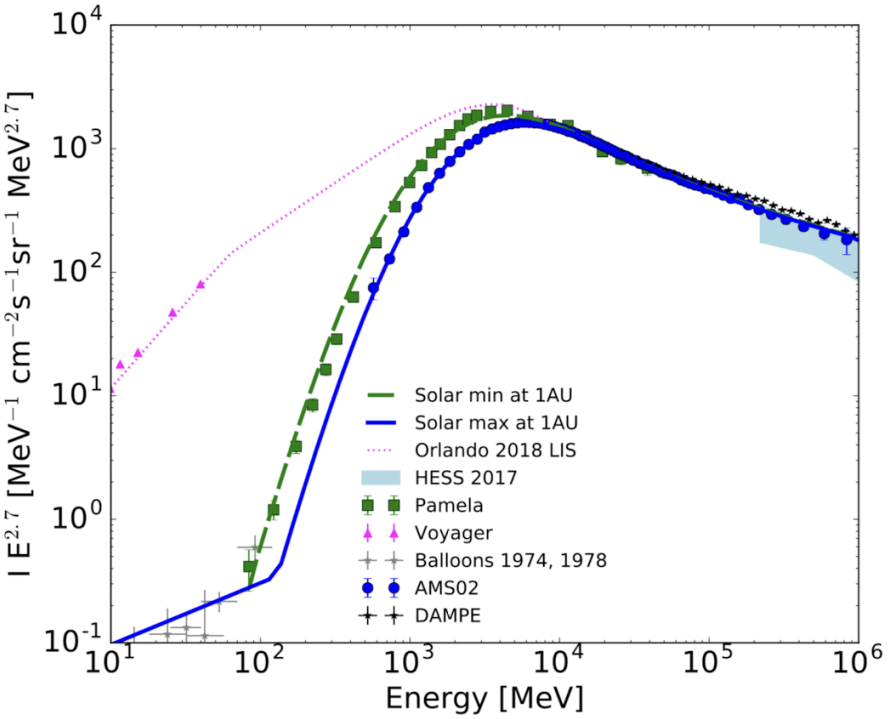

Figure 2.5.: All electron spectrum models for a distance of 1 AU to the Sun based on PAMELA (green) and AMS-02 (blue) data. Both models are fitted to the AMS-02 data above 40 GeV and to Balloon data from 1974 and 1978 below 100 MeV. The local interstellar spectrum is shown by the magenta line together with data from Voyager. HESS 2017 and DAMPE data are also shown. Figure taken from (Orlando et al., 2021).

To approximate the solar radiation field, the Sun is treated as a blackbody with $T = 5777\,\mathrm{K}$ as shown in Fig. 2.3. To obtain the extended photon density distribution near the Sun, integration is performed over the solid angle of the solar surface (Orlando et al., 2021):

$$n_{ph}(E_{ph}, r) = 0.5 n_{BB}(E_{ph})[1 - \sqrt{1 - (R_\odot/r)^2}] \tag{2.8}$$

Here E_{ph} is the photon energy, n_{BB} is the blackbody photon density, and $R_\odot$ is the solar radius. Using these parameters, Orlando et al. (2021) calculated the solar IC spectrum using the models from Fig. 2.5 and by applying the Klein-Nishina cross section σ_{KN} to take into account the relativistic effects, as shown in Fig. 2.6.

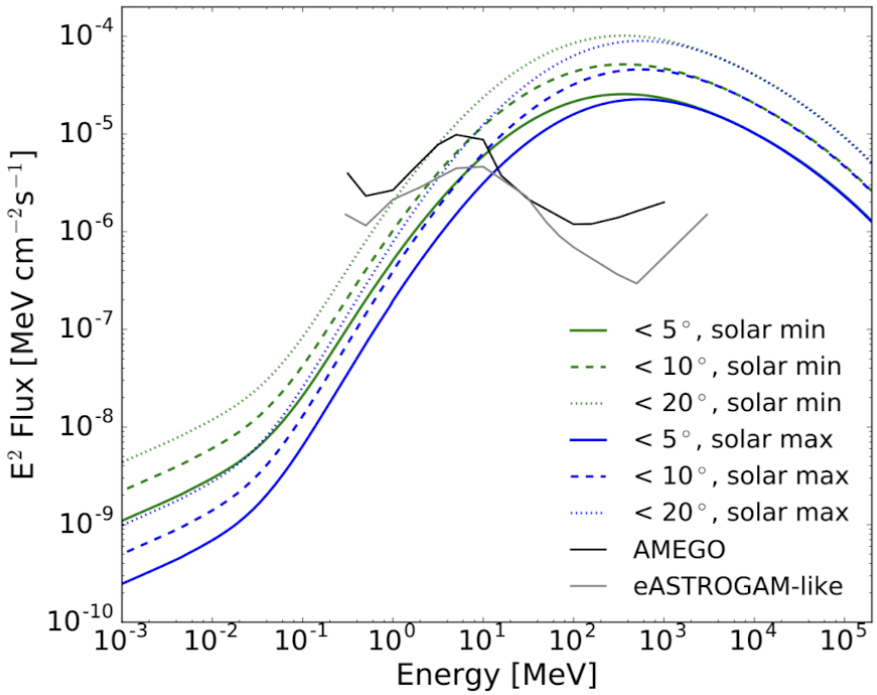

Figure 2.6.: Calculated solar IC flux by Orlando et al. (2021). The green lines represent calculations using the solar minimum electron spectrum, while the blue lines use the solar maximum electron spectrum from Fig. 2.5. For both electron spectra, the IC spectrum was determined for three different elongation angles: 5°, 10° , and 20°. The AMEGO (for five years observation time) and eASTROGAM (for one year observation time) sensitivities are also shown.

The IC flux for different angles clearly shows the extended emission around the Sun. Fig. 2.6 shows that IC scattering produces photons with energies ranging from keV to TeV. The maximum radiation occurs in the GeV range, and beyond this the influence of the Sun on the CR electrons can be neglected. The IC flux for values $< 1\,\mathrm{GeV}$ represents an upper estimate of the true flux, as the increased modulation of the CR electrons closer to the Sun has not been taken into account.

2.2.2. Hadronic Emission

An essential contribution to the solar disc emission is provided by the interaction of Cosmic Particles with the solar atmosphere and surface. When incoming high-energy cosmic primary particles, mainly protons, alpha particles, and electrons, encounter the solar atmosphere, they interact with the atomic nuclei in the atmosphere, thereby producing secondary particles such as pions, kaons, and muons. These particles then decay through secondary processes. During this so-called hadronic shower, numerous neutral pions π^0 decay into two gamma photons (Seckel et al., 1991). Through pair production, these photons now generate electron-positron pairs, thus initiating an electromagnetic shower. The deflection of these particles by the atomic nuclei of the atmosphere and the resulting

bremsstrahlung give rise to additional photons, which in turn create particle pairs. Additionally, electromagnetic showers are also directly triggered by cosmic-ray electrons and by bremsstrahlung of charged hadrons generated as secondary particles. This shower continues to grow until the particles involved no longer have enough energy to produce further particles. A portion of the gamma-rays produced in these cascades no longer contribute to further decay processes, but instead exit the solar atmosphere, thereby contributing to the Sun's gamma-ray spectrum.

Modulation of the Hadronic Emission

Together with the spectrum of cosmic primary particles and the Sun's modulation, the density and composition of the solar atmosphere are the most important model parameters for determining the gamma spectrum.

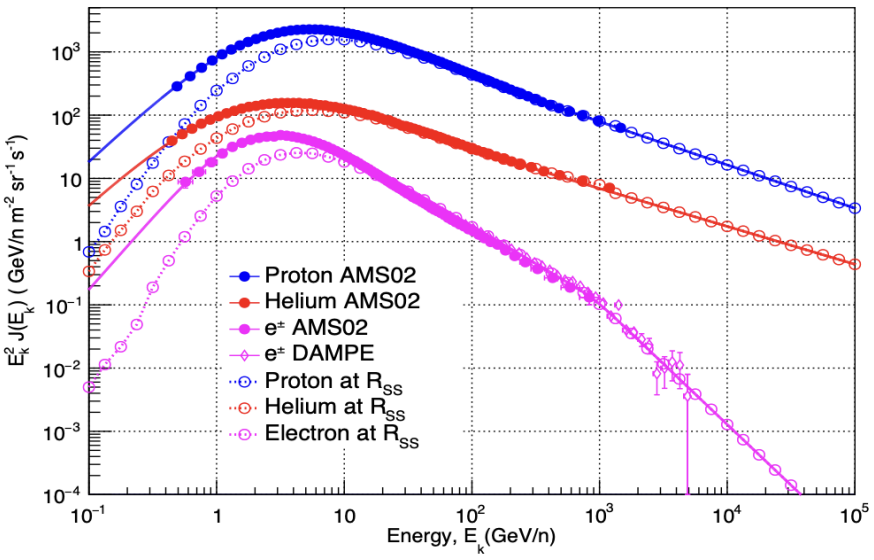

Figure 2.7.: Intensity of cosmic protons, helium and electrons compared to their kinetic energy. They are all fitted to the AMS-02 data and the electrons added to the DAMPE data obtained at the distance $r = 1\,\mathrm{AU}$. The modification of the spectrum at the distance $R_{\mathrm{SS}} = 2.5\,R_{\odot}$ is also shown. Figure taken from (Mazziotta et al., 2020).

Fig. 2.7 shows that protons and helium make up a significantly larger portion of cosmic rays than electrons. Additionally, the influence of the Sun on the spectrum of these particles can be seen. It is also apparent that this effect decreases as the particles become more energetic. The density of the solar atmosphere has two important influencing factors: On one hand, a high density is beneficial for increasing the interaction probability of the particles with the atmosphere; on the other hand, a dense atmosphere absorbs more gamma-rays, making their escape less likely (Seckel et al., 1991). Additionally, the Sun's magnetic field near its surface has two different effects on the primary particles. A strong

magnetic field reduces the likelihood of low-energy particles reaching the Sun because they are deflected, which decreases the production of low-energy gamma radiation. However, high-energy particles are not deflected by the magnetic field but are instead forced into a circular path, which increases the interaction probability with the solar atmosphere and enhances the production of higher-energy gamma radiation (Mazziotta et al., 2020). The modeled solar spectrum in Fig. 2.8 shows that analogous to Fig. 2.7, protons contribute the most to the gamma spectrum. The 511 keV peak due to positron annihilation and the 2.2 MeV peak due to neutron capture are clearly visible. The modeled spectrum also shows good agreement with the measured Fermi-LAT data of the Sun, although the spectrum lies slightly below the data, which may be due to the unaccounted disc emission from IC radiation (Mazziotta et al., 2020).

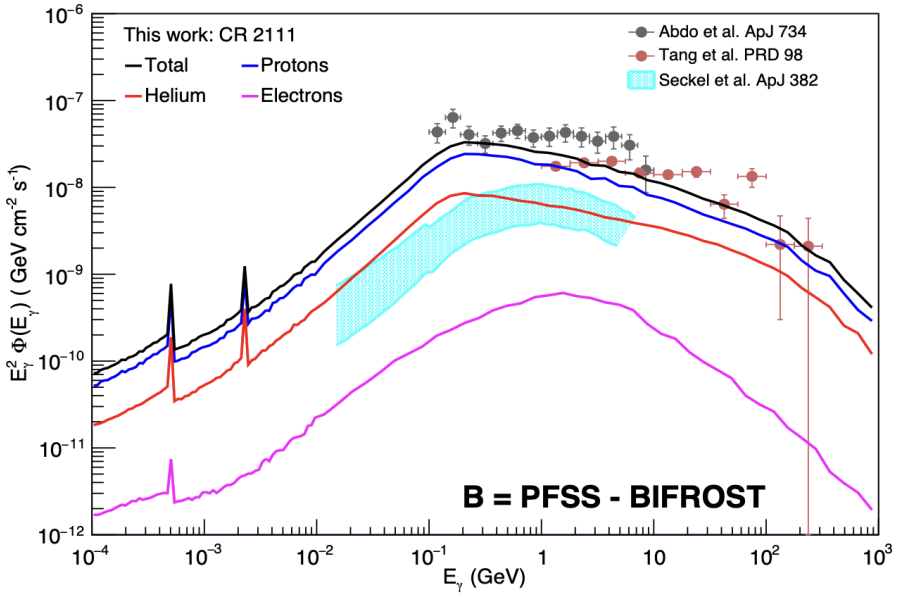

Figure 2.8.: Mazziotta et al. (2020) modeled the gamma radiation from the solar disc due to the interaction of the solar atmosphere with cosmic protons, helium and electrons. The total spektrum is the sum of the three different spectra. Also shown as gray and red points are two different Fermi-LAT data and a previous model for the gamma-ray spectrum from (Seckel et al., 1991).

2.2.3. Reflected cosmic X-ray background radiation

The Sun is also a source of high-energy radiation because the already existing Cosmic X-ray Background (CXB) radiation hits the Sun's atmosphere and is reflected by it. The key processes that must be considered are photoelectric absorption, Rayleigh and Compton scattering, and fluorescence (Churazov et al., 2008).

In photoelectric absorption, photons are absorbed by the inner electrons of an atom, causing the electron to be ejected from the atom. This effect reduces the number of incoming photons and consequently the number of reflected photons. This process mainly occurs

for energies less than 100 keV, as the cross-section becomes negligibly small for higher energies (Churazov et al., 2008).
Photoelectric absorption additionally leads to the ejection of an inner electron creating a vacancy in the inner electron shell, which can be filled by an outer electron. This transition emits a photon corresponding to the energy difference between the two electron states. This effect is known as fluorescence. These photons contribute to the reflection spectrum, although they are not directly reflected CXB photons.
Rayleigh scattering occurs when photons interact with particles such as atoms or molecules that are significantly smaller than the photon wavelength. Due to the electric field of the radiation, these particles become polarized and begin to oscillate at the photon frequency. As a result, these particles behave like small dipoles, re-emitting the absorbed radiation while maintaining the photon frequency. This scattering process reflects part of the incoming CXB spectrum back from the Sun. As the wavelength of high energy photons is already very small, this effect is only significant for radiation below 100 keV, as the wavelength of higher-energy radiation becomes too small to interact with particles in this way (Churazov et al., 2008).
For the reflected higher-energy CXB spectrum, Compton scattering plays a crucial role. As discussed in Chapter 2.2.1, the photon scatters off an electron, reducing the energy of the photon. From an energy of $\gtrsim$ 40 keV, this process dominates the reflected CXB spectrum, and above about 100 keV, almost exclusively contributes to the reflection of the incoming CXB radiation (Churazov et al., 2008).

Modulation of reflected CXB Emission

Taking into account the CXB spectrum approximated by Gruber et al. (1999) and the density and composition of the solar atmosphere, Churazov et al. (2008) determined the reflected CXB spectrum, which is shown in Fig. 2.9.
Compared to the original CXB spectrum, the dominant photoelectric absorption is clearly visible at lower energies. The fluorescence lines characteristic of the photospheric composition appear at energies between 1 keV and 10 keV, with a prominent iron fluorescence peak at 6.4 keV. The energy spectrum peaks at about 30 keV, where the cross sections for Rayleigh and Compton scattering exceeds that for photoelectric absorption (Churazov et al., 2008).

2.2.4. Solar Albedo Model

Peterson et al. (1966) present a model of the quiet solar gamma-ray emission calculated from an estimate based on measurements of the background radiation from the terrestrial albedo. These data were obtained at an atmospheric depth of $3.6\,\mathrm{g\,cm^{-2}}$. The measurements were extrapolated to zero depth, corrected for the angle of observation and the solid

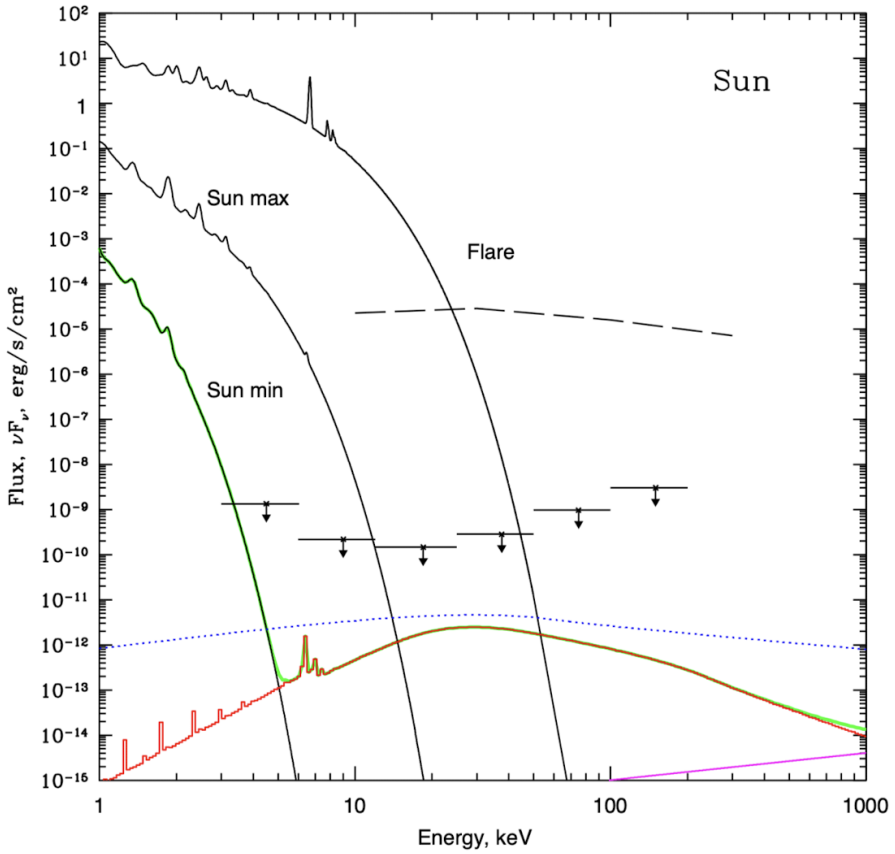

Figure 2.9.: The red line shows the reflected CXB spectrum from the solar disc. The typical thermal corona emission are shown during solar minimum, maximum and flares ,and the nonthermal component of a strong flare is indicated (dashed line). The upper limits of the quiet Sun emission obtained by RHESSI show the constraints of the spectrum up to 200 keV (Hannah et al., 2007). The blue dotted line shows the pure CXB spectrum integrated over the Sun's solid angle. The magenta line shows the disc emission due to the interaction of CR. Figure taken from (Churazov et al., 2008).

angle fraction occupied by the Sun. This results in an estimated solar flux, which is shown in Fig. 2.10 together with the other models from above. The solar albedo model predicts the highest flux. This expected model includes a combination of hadronic emission and CXB emission. Since the Earth's photon field is significantly weaker than that of the Sun, the model includes little to no IC emission from the Sun. Between 20–100 keV the solar albedo and the CXB reflection are close together. From an energy of about 1 MeV the solar albedo decreases parallel to the Hadronic emission and the 511 keV peak is visible but the 2.2 MeV was not included in the model calculation.

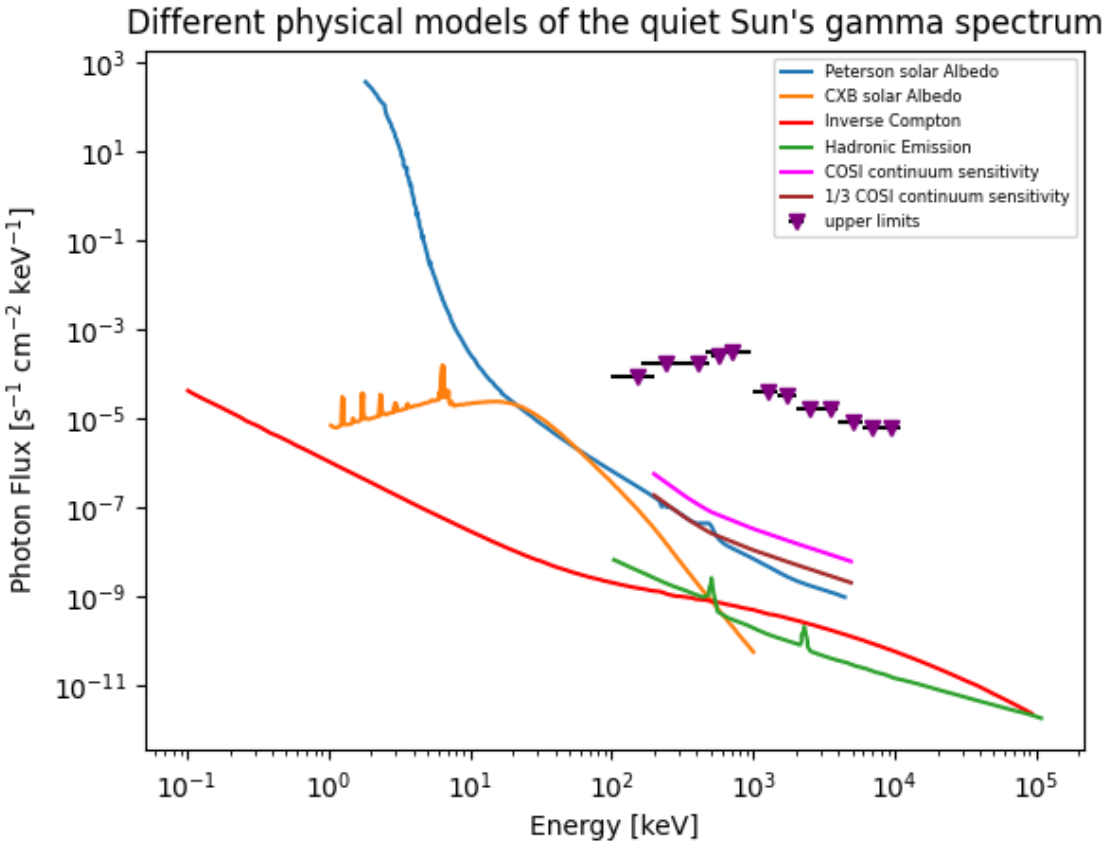

Figure 2.10.: The expected solar albedo from Peterson et al. (1966), the reflected CXB emission from Churazov et al. (2008), the inverse compton radiation from Orlando et al. (2021) and the calculated hadronic emission from Mazziotta et al. (2020). The Peterson albedo is shown together with the coronal x-ray emission which smoothly joins the albedo at about 10 keV. *COSI*'s 3σ and 1σ continuum sensitivity and the upper limits from chapter 3.3 are shown.

2.3. Measurements of the quiescent Sun from keV to MeV

The energy range from hard X-ray radiation to lower MeV radiation from the quiet Sun remains elusively studied. Measurements in this range were primarily optimized for observing solar flares and thus were not suitable for measuring such small fluxes (Hannah et al., 2007). Previous measurements aimed at determining the quiescent solar flux only resulted in upper limits for the spectrum. These upper limits completely cover the energy range from 3 keV to 11 MeV.

2.3.1. Balloon Measurements

Frost et al. (1966) describe a balloon-borne detector system, which was launched over Minneapolis on June 10, 1962 and ascended to an altitude of approximately 39 km. This campaign reduced the obscuring of the gamma-ray signals due to absorption and scattering effects in the atmosphere. The detector system included a NaI(Tl) scintillation crystal, surrounded by CsI(Tl) collimator shield, which minimized background radiation from wide angles and enhanced the directional sensitivity of the detector towards its orientation (Frost et al., 1966).

The detector was oriented downward, upward, and horizontally to obtain information about the radiation from different directions. Then, the detector was pointed at the Sun for 25 min and subsequently rotated by 180° while maintaining the same elevation. In this new orientation, measurements were taken for 20 min to obtain the background flux, which needs to be subtracted from the direct solar measurement. During the 8-hour flight phase at this altitude, eight such measurement processes were conducted. The data was obtained at an average zenith angle of 35° and an average mass density of $3.5\,\mathrm{g\,cm^{-2}}$. Table 2.1 shows the measured count rate towards and away from the Sun averaged over the eight periods for different energy intervals, corrected for deadtimes, atmospheric depth and channel widths (Frost et al., 1966).

Energy range, keV	Towards Sun, (c/s)	Away from Sun, (c/s)	Differential Rate, (c/s)	Upper limit Flux, $\mathrm{cm^{-2}s^{-1}MeV^{-1}}$
163-325	1.901 ± 0.036	1.928 ± 0.041	-0.027 ± 0.056	0.166
325-488	0.961 ± 0.027	0.973 ± 0.030	-0.012 ± 0.042	0.171
488-651	0.704 ± 0.023	0.705 ± 0.026	0.001 ± 0.037	0.263
651-774	0.374 ± 0.015	0.366 ± 0.016	0.008 ± 0.020	0.307

Table 2.1.: Measured counts per second towards the Sun and away from the Sun for different energy intervals obtained from (Frost et al., 1966). These values were used to determine upper limits for the solar flux.

The data show no significant difference between the measurements towards and away from

the Sun. The authors estimated upper limits for the solar flux for the four energy bins at a 95% confidence level, as shown in Table 2.1. For the calculation of the upper limits, the measured data had to be corrected for the detector efficiency for a continuous spectrum. Peterson et al. (1966) describe two balloons carrying two similar detector systems compared to the Measurement from Frost et al. (1966), which were launched on February 18, 1966 from Phoenix. The two detectors were designed for two different energy ranges. The ranges covered were (17.5–185) keV and (1.0–11.0) MeV. The balloons each reached a

Energy range, keV	Typical Counting Rates, (c/s)	Upper limit Flux, counts/cm^{-2}s^{-1}MeV^{-1}
17.5-37.5	0.278 ± 0.005	0.81
37.5-60.0	0.252 ± 0.005	0.27
60.0-80.0	0.173 ± 0.003	0.15
80.0-135.0	0.414 ± 0.005	0.09
135.0-185.0	0.255 ± 0.003	0.06
$(1.0 - 1.5) \cdot 10^3$	10.7 ± 0.05	$4.0 \cdot 10^{-3}$
$(1.5 - 2.0) \cdot 10^3$	6.30 ± 0.04	$3.2 \cdot 10^{-3}$
$(2.0 - 3.0) \cdot 10^3$	8.24 ± 0.04	$1.6 \cdot 10^{-3}$
$(3.0 - 4.0) \cdot 10^3$	5.63 ± 0.05	$1.6 \cdot 10^{-3}$
$(4.0 - 6.0) \cdot 10^3$	7.26 ± 0.04	$0.8 \cdot 10^{-3}$
$(6.0 - 8.0) \cdot 10^3$	4.11 ± 0.03	$0.6 \cdot 10^{-3}$
$(8.0 - 11.0) \cdot 10^3$	4.06 ± 0.03	$0.6 \cdot 10^{-3}$

Table 2.2.: Measured count rate of the atmospheric background at an atmospheric depth of $3.5\,\mathrm{g\,cm^{-2}}$ and $3.6\,\mathrm{g\,cm^{-2}}$ for different energy ranges. The resulting upper limits of the solar flux calculated by Peterson et al. (1966) are listed.

floating level at an atmospheric depth of $3.5\,\mathrm{g\,cm^{-2}}$ and $3.6\,\mathrm{g\,cm^{-2}}$. The values for the solar flux and the background were measured similar to Frost et al. (1966), maintaining the elevation angle and rotating the apparatus by 180°. Again, there was no significant difference between the background and Sun-facing measurements. Therefore, after correcting for atmospheric depth, dead time, and channel width, limits of the quiet Sun spectrum at a 95% confidence level were determined for reasonable energy ranges, as shown in Table 2.2. In order to compare the obtained upper limits with previous measurements, Peterson et al. (1966) did not correct them for efficiency. The upper limits from Table 2.2 joins smoothly onto the uncorrected values from Frost et al. (1966). The upper limits between 100 and 11000 keV are shown in Fig. 2.10 together with the models from section 2.2, which are many orders of magnitudes below the upper limits.

2.3.2. Satellite observations

Equipped with germanium detectors, the Reuven Ramaty High-Energy Solar Spectroscopic Imager (*RHESSI*) was launched in 2002 (Smith et al., 2003). The main mission

goal was to explore the physical processes inside solar flares. The measurements were conducted by Hannah et al. (2007) during periods when the Geostationary Operational Environmental Satellite *GOES 12* measured a flux within the region 1–8 below $10^{-8}\,\mathrm{W\,m^{-2}}$, indicating a quiet Sun. In order to improve the chance of distinguishing the quiet solar flux from the cosmic and instrumental background, an offpointing technique called fan-beam modulation was used. *RHESSI* was offpointed between 0.4° and 1° from the Sun's center. The goal of this approach was to create a periodicity in the measured solar emission and therefore recognize it better in the data. Since the angle of incidence of the incoming radiation affects how much of it is transmitted through *RHESSI*'s grid collimators, the slight off-pointing and the rotation of the spacecraft ensure that two transmission maxima are generated per rotation when the grids are parallel to the line between the Sun and *RHESSI*'s orientation Hannah et al. (2007). This results in only the incoming solar emission being periodically modulated and not the constant isotropic background flux. The observation was carried out during seven quiescent periods for a total of 45 days. As shown in Table 2.3 the measurements result in new upper limits for the energy range $(3-200)\,\mathrm{keV}$. Therefore *RHESSI* improved the upper limits obtained by the lower energetic balloon measurement from Peterson et al. (1966). The upper limits obtained by *RHESSI* are shown in Fig. 2.9.

Energy range, keV	Weighted Mean, $10^{-4}\,\mathrm{photons\,s^{-1}\,cm^{-2}\,keV^{-1}}$	Upper limit Flux 2σ, $10^{-4}\,\mathrm{photons\,s^{-1}\,cm^{-2}\,keV^{-1}}$
3-6	330.99	414.50
6-12	−5.24	16.92
12-25	−0.73	2.68
25-50	0.14	1.26
50-100	0.74	1.08
100-200	−0.97	0.84

Table 2.3.: Measured mean value of the obtained solar flux and the calculated 2σ upper limits for different energy ranges by Hannah et al. (2007).

Although there are other satellites operating in this gamma-ray region, no additional upper limits have been established by satellite measurements. The INTEGRAL spacecraft is never pointed at the Sun to avoid damaging its sensitive instruments. The Gamma Ray Burst Monitor (GBM) is optimised to detect short and intense signals such as bursts. This makes it difficult to measure the Sun as a weak continuous source, but it would be possible. The COMPTEL and OSSE instruments have observed the Sun, which could lead to new, more constraining upper limits, but this has not yet been evaluated.

3. Statistical Analysis of Previous Measurements

3.1. Probability theory framework

Bayesian statistics relies on probability theory as its basis. This section will explore the core concepts of probability theory for understanding and applying model fits to gamma-ray spectra in particular. In statistics, probabilities are utilized to quantify uncertainties related to model parameters and predictions. Unlike frequentism, that views probability as the long term frequency of events, Bayesian statistics interpret probability as a measure of belief or confidence in an event or hypothesis given available (or unavailable) information (Bishop, 2007). This perspective enables us to integrate knowledge and update our beliefs with data. To effectively utilize methods in model fitting tasks it is essential to comprehend several fundamental concepts in probability theory.

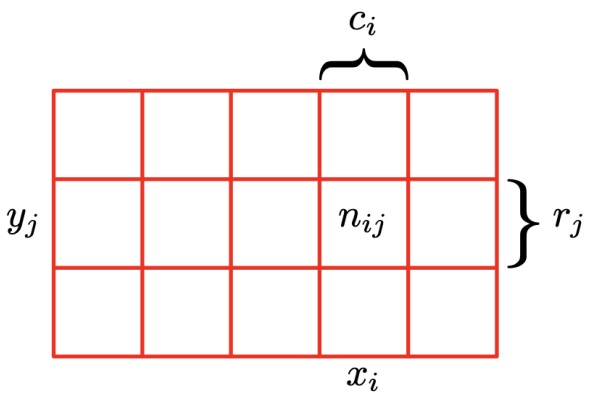

Figure 3.1.: Table of two random variables X and Y. Here c_i/r_j is the number of instances that are attributed to the value x_i/y_j of X/Y and n_{ij} is the number of instances that are attributed to the value x_i and y_j. Figure taken from (Bishop, 2007).

Fig. 3.1 shows the two random variables X and Y and helps to illustrate the sum and product rules of probability. The probability that X and Y take on a specific value independently of each other is written as $p(X = x_i) = c_i/N$ and $p(Y = y_j) = r_j/N$. For the probability that X and Y simultaneously take on a value with respect to the other variable, we write $p(X = x_i, Y = y_j) = n_{ij}/N$, where N is the total number of instances. This is known as the joint probability, and it holds that $p(X, Y) = p(Y, X)$. From these

definitions, we can derive the summation rule for probabilities. Since c_i is $c_i = \sum_j n_{ij}$ one can write:

$$p(X = x_i) = \sum_j p(X = x_i, Y = y_j). \tag{3.1}$$

Now, if we fix a value of X and are interested in the probability that Y takes on a specific value under this term, this is referred to as the conditional probability $p(Y = y_j|X = x_i) = \frac{n_{ij}}{c_i}$. Fixing X to a certain value reduces the total number N to c_i, which leads to the replacement of N with c_i compared to $p(X, Y)$. To revert from the conditional probability back to the joint probability, $p(Y|X)$ must be multiplied by $\frac{c_i}{N}$, resulting in $\frac{n_{ij}}{c_i} \cdot \frac{c_i}{N} = \frac{n_{ij}}{N}$. From this we can derive the product rule for probabilities:

$$p(X = x_i, Y = y_j) = p(Y = y_j|X = x_i)p(X = x_i). \tag{3.2}$$

Summarized, the two rules can be written as follows:

$$\text{Sum rule} \quad p(X) = \sum_Y p(X, Y) \tag{3.3}$$

$$\text{Product rule} \quad p(X, Y) = p(Y|X)p(X). \tag{3.4}$$

Combining the product rule with the property of joint probability, we obtain by rearranging the equation $p(Y|X)p(X) = p(X|Y)p(Y)$:

$$\textbf{Bayes' theorem} \quad p(Y|X) = \frac{p(X|Y)p(Y)}{p(X)}. \tag{3.5}$$

Bayes' theorem can be seen as an ensemble between prior knowledge about a random variable and new information gained from a measurement, leading to an updated probability for the occurrence of this random variable (Bishop, 2007). The knowledge $p(Y)$, which exists about Y before any measurement is conducted, is called the prior probability. The probability $p(Y|X)$ of a random variable after incorporating the information from the measurement is called the posterior probability and $p(X|Y)$ is called the likelihood that takes the measurement into account. The denominator $p(X)$ serves as the normalization constant, ensuring that the posterior distribution integrates to one.

3.2. Bayesian model fitting

The goal of model fitting is to predict the target variable t for new input values x based on a set of known data of N input values $\mathbf{x} = (x_1, \ldots, x_N)^T$ and their corresponding target values $\mathbf{t} = (t_1, \ldots, t_N)^T$ with the uncertainty $\boldsymbol{\sigma} = (\sigma_1, \ldots, \sigma_N)^T$. The uncertainty over the target variable's value is expressed using a probability distribution. Assuming that given

x, the corresponding t follows a Gaussian distribution with a mean equal to the fitting function value $y(x, \mathbf{w})$, where $\mathbf{w}$ is the parameter vector, as shown in Fig. 3.2 (Bishop, 2007). Therefore, we can write the probability with the precision parameter $\beta = \frac{1}{\sigma^2}$ as:

$$p(t|x, \mathbf{w}, \beta) = \mathcal{N}(t|y(x, \mathbf{w}), \beta) \tag{3.6}$$

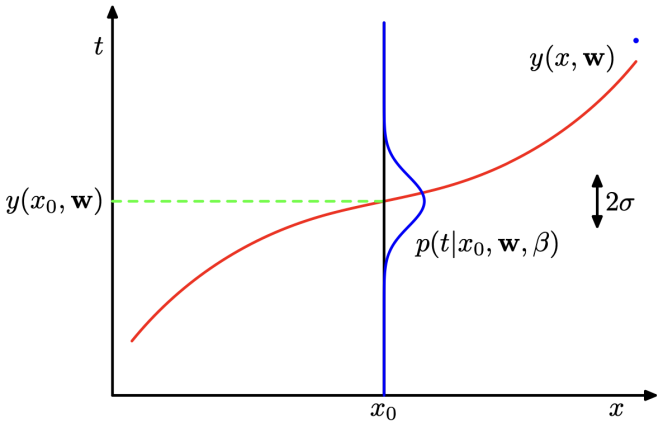

Figure 3.2.: Gaussian distribution of a target variable t at the input variable x_0. The red curve shows the fitted function $y(x, \mathbf{w})$ and the mean of the distribution equals the value $y(x_0, \mathbf{w})$. Figure taken from (Bishop, 2007).

In order to obtain $y(x, \mathbf{w})$ we need to determine the parameters $\mathbf{w}$ by using the known data set $(\mathbf{x}, \mathbf{t})$. Under the assumption that the probability distribution of one measured data point following the fitted model equals a Gaussian distribution one can write according to 3.6 (Bishop, 2007):

$$p(t_i|x_i, \mathbf{w}, \beta_i) = \mathcal{N}(t_i|y(x_i, \mathbf{w}), \beta_i) \tag{3.7}$$

Now under the condition that the single values of the data set are independent of each other, the product rule 3.4 leads to the likelihood function that the whole data set follows $y(x, \mathbf{w})$:

$$p(\mathbf{t}|\mathbf{x}, \mathbf{w}, \boldsymbol{\beta}) = \prod_{i}^{N} \mathcal{N}(t_i|y(x_i, \mathbf{w}), \beta_i) \tag{3.8}$$

The likelihood function indicates how proper the data set follows $y(x, \mathbf{w})$ for different settings of $\mathbf{w}$. As we want to get the most likely value of $\mathbf{w}$ we have to maximize $p(\mathbf{t}|\mathbf{x}, \mathbf{w}, \boldsymbol{\beta})$ with respect to $\mathbf{w}$. Since $p(t_i|x_i, \mathbf{w}, \beta_i)$ can take very small values, the product of these takes even smaller values. Therefore instead of $p(\mathbf{t}|\mathbf{x}, \mathbf{w}, \boldsymbol{\beta})$, $-\ln(p(\mathbf{t}|\mathbf{x}, \mathbf{w}, \boldsymbol{\beta}))$ is maximized since the position of the maximum will not change (Bishop, 2007).

$$\ln(p(\mathbf{t}|\mathbf{x}, \mathbf{w}, \boldsymbol{\beta})) = \sum_{i}^{N} \ln(\mathcal{N}(t_i|y(x_i, \mathbf{w}), \beta_i)) = -\frac{\beta}{2} \sum_{i}^{N} \frac{\beta_i}{2} (y(x_i, \mathbf{w}) - t_i)^2 + \text{const.} \tag{3.9}$$

After completing this, one can now make predictions of the target variable t for a given x. This predictions are stated as a predictive probability distribution over t 3.6, since we work with a probabilistic model rather than a point estimation for t.
If we now additionally have prior information $p(\mathbf{w})$ about the parameter vector $\mathbf{w}$, the posterior distribution of $\mathbf{w}$ can be written in accordance with Bayes' theorem as follows:

$$p(\mathbf{w}|\mathbf{x},\mathbf{t}) \propto p(\mathbf{t}|\mathbf{x},\mathbf{w})p(\mathbf{w}) \qquad \text{(posterior} \propto \text{likelihood} \times \text{prior)} \tag{3.10}$$

Therefore the posterior distribution leads to the probabilistic model of $\mathbf{w}$ (Bishop, 2007). Since the exact form of $p(\mathbf{w}|\mathbf{x},\mathbf{t})$ is usually difficult to compute analytically, we need to approximate the posterior distribution. This is done by Monte Carlo sampling over p($\mathbf{t}$|$\mathbf{x}$,$\mathbf{w}$)p($\mathbf{w}$) to obtain the distribution $p(\mathbf{w}|\mathbf{x},\mathbf{t})$.

3.3. Fitting of the solar spectrum from 100 keV to 10 MeV

Using the measured upper limits of the solar spectrum from section 2.3.1 and the fitting procedure from section 3.2 we can now fit the solar spectrum so that it describes the entire range and still takes into account the upper limits. Since no significant flux was detected, the mean photon fluxes in the respective energy ranges can be set to zero. In more detail, this procedure would require a so-called "survival analysis" (Yu et al., 2024), but since the upper limits are far from the theoretical predictions, a value close to or at zero will suffice to discuss the results here. In addition, we will use a 1σ uncertainty from the quoted upper limits as shown in Tab. 3.1. We will further constrain ourselves to the energy bands for the upcoming COSI mission (chapter 4), ranging from 100 keV to 10 MeV.

Energy range keV	**Photon flux** $\frac{10^{-4}}{\mathrm{s\,cm^2\,keV}}$	**Errorbar** $\frac{10^{-4}}{\mathrm{s\,cm^2\,keV}}$	**Energy range** keV	**Photon flux** $\frac{10^{-4}}{\mathrm{s\,cm^2\,keV}}$	**Errorbar** $\frac{10^{-4}}{\mathrm{s\,cm^2\,keV}}$
100 - 200	0	0.42	1500 - 2000	0	0.16
163 - 325	0	0.83	2000 - 3000	0	0.08
325 - 488	0	0.855	3000 - 4000	0	0.08
488 - 651	0	1.315	4000 - 6000	0	0.04
651 - 774	0	1.535	6000 - 8000	0	0.03
1000 - 1500	0	0.20	8000 - 11000	0	0.03

Table 3.1.: The flux values used for fitting the gamma-ray spectrum of the quiet Sun, along with the associated error bars.

In the papers of Peterson et al. (1966), we estimate that the uncertainties may be largely underestimated given the limits are from the 1960s. We increase the uncertainties by a

factor of 10 to obtain conservative estimates in the following. For the fitting functions, a power-law was used for the continuum emission, and a Gaussian was applied for a separate analysis of the 511 keV line.

$$\text{Prower-law:} \quad a \left(\frac{x}{x_{\text{piv}}} \right)^b \tag{3.11}$$

$$\text{Gaussian:} \quad \frac{c}{\sigma\sqrt{2\pi}} \exp\left(-\frac{(x - x_0)^2}{2\sigma^2} \right). \tag{3.12}$$

The scaling factors a, c and the power-law index b are the fitting parameters. The standard deviation σ is set to 5 keV, since the Sun is a hot object, the observed line flux is Doppler-shifted, leading to an uncertain broadening. The expected value is fixed at $x_0 = 511\,\text{keV}$ and the pivot point, where the power-law is normalized is set to $x_{\text{piv}} = 1000\,\text{keV}$. As there is no prior knowledge of these parameters, a flat prior distribution is used for all parameters. Samples are generated from the resulting distributions according to section 3.10. The (MCMC) simulation was carried out using the Python package `emcee`[1]. Thirty walkers, or starting samples, were used to sample the distribution. Each starting sample generated 2,000 samples, giving a total of 60,000 samples. Since the initial samples are primarily influenced by the initial values and not the target distribution, these so-called 'burn-in" samples were discarded, as shown in Fig. 3.3.

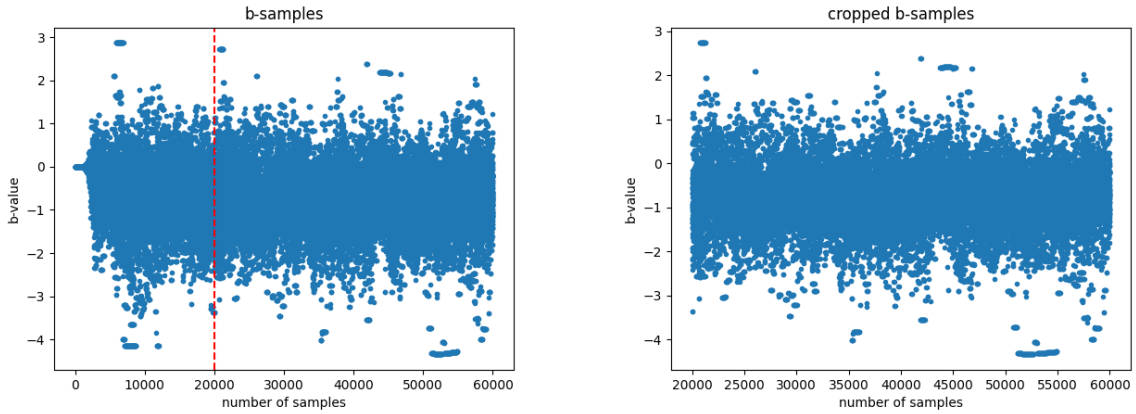

Figure 3.3.: Samples drawn from the distribution of the power-law index b. The left Figure shows the whole 60000 samples with the burn-in samples at the beginning not following the distribution. The red line indicates the cut at 20000 which marks the neglected and used samples. The figure on the right shows the used samples.

The samples obtained for the three fit parameters are shown in Fig. 3.4 with the mean values $a = (0 \pm 3) \times 10^{-6}\,\text{s}^{-1}\,\text{cm}^{-2}\,\text{keV}^{-1}$, $b = -0.79 \pm 0.64$, and $c = (0.1 \pm 2.2) \times 10^{-2}\,\text{s}^{-1}\,\text{cm}^{-2}\,\text{keV}^{-1}$. The histograms exhibit a nearly-Gaussian shape of the sampled posterior distributions. The narrow distribution of the power-law amplitude, with a median of $0\,\text{s}^{-1}\,\text{cm}^{-2}\,\text{keV}^{-1}$, as expected from the zero fluxes. The median power-law index

[1] `https://emcee.readthedocs.io/en/stable/`

reflects the decreasing trend of the upper limits, and the median amplitude of the Gaussian is just below the $2\,\sigma$ upper limit of the 511 keV energy range.
Now, we can evaluate models for the solar spectrum according to the posterior sampling. Therefore, a posterior model is created for each tuple of samples. Since these models follow the posterior distribution, each model now lies within a certain percentile range, which therefore indicates its prior-weighted likelihood. The obtained models are shown in Fig 3.5 divided into the 68th, 95th and 99.7th percentile. One can see that all models within the 95th percentile range lie below the $2\,\sigma$ upper limits, except for the 511 keV peak. Fig 3.5 also shows that no positive power-law indices lie within the 68th percentile range, but the 511 keV lines within the 68th percentile extend about an order of magnitude beyond the upper limit of the 511 keV range. This is reasonable because we assumed a line width of 5 keV, but the energy bin in which the annihilation is found has a width of 163 keV, which means one can "hide" larger line fluxes which may be drowning in the broad energy bins from the previous measurements.
Fig. 3.6 shows the different models from section 2.2 within the fitted solar flux. One can see that all the theoretical models lie within the 68th percentile range. The solar albedo model, which predicts the highest flux, lies between 1.5 and 3 orders of magnitude below the edge of the 68th percentile range. The energy range from 100 to $\sim$ 500 keV has the highest potential for being constrained if the upper limits could be lowered with more observation time. While this range might offer the best chance for constraints, since no further observation time is available, no additional constraints can currently be applied.
Given the model fit, the 511 keV line flux is at most $5.8 \times 10^{-4}\,\mathrm{s^{-1}\,cm^{-2}\,keV^{-1}}$ for the quiet sun. The total flux from 100 to 10000 keV, using the mean power-law index and one sigma of the power-law amplitude, is $1.53 \times 10^{-2}\,\mathrm{s^{-1}\,cm^{-2}\,keV^{-1}}$. These values are far above the expected models, but would be clearly seen with an instrument like *COSI* (see chapter 4).

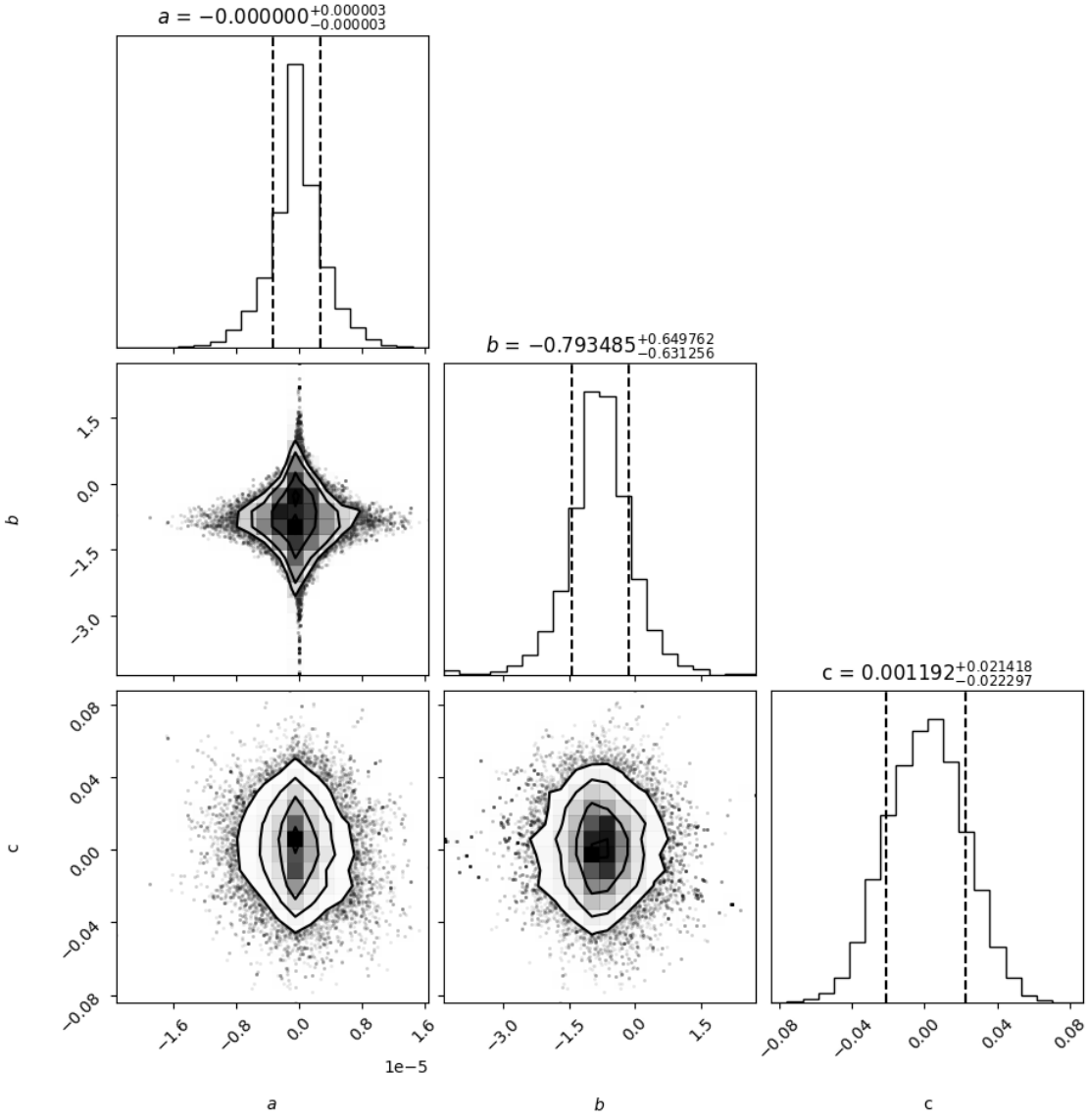

Figure 3.4.: The corner plot of the fit parameters a, b and c shown as histograms. The dashed lines mark the range in which 68 percent of the samples are found around the mean value. The joint posterior probability for each variable is also shown.

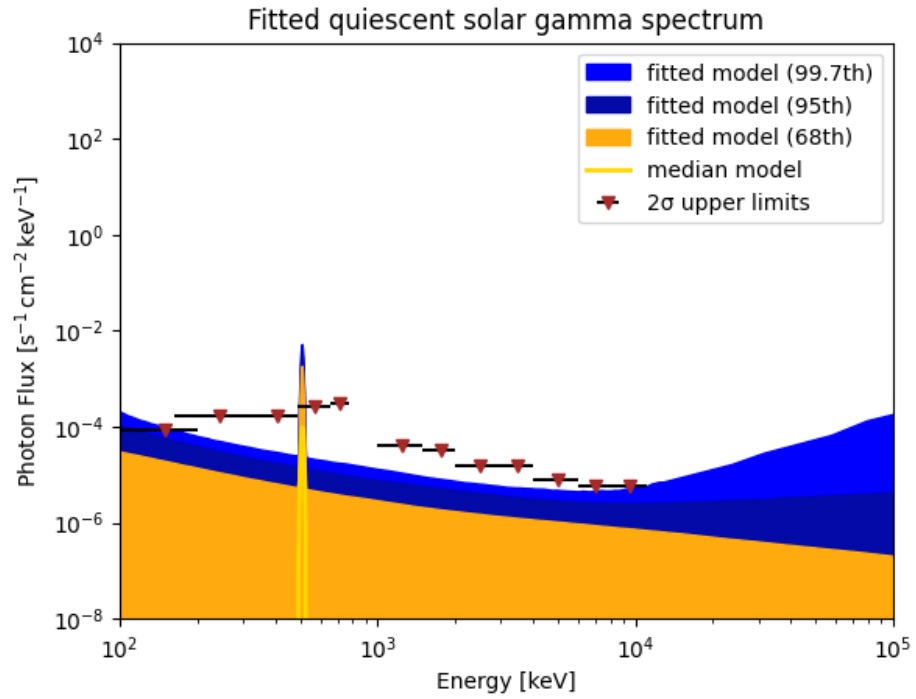

Figure 3.5.: Bayesian fit of the quiescent solar gamma-ray spectrum. The evaluated models within the 68th, 95th and 99.7th percentile and the median model are shown. Also shown are the $2\,\sigma$ upper limits of the quiet Sun's flux.

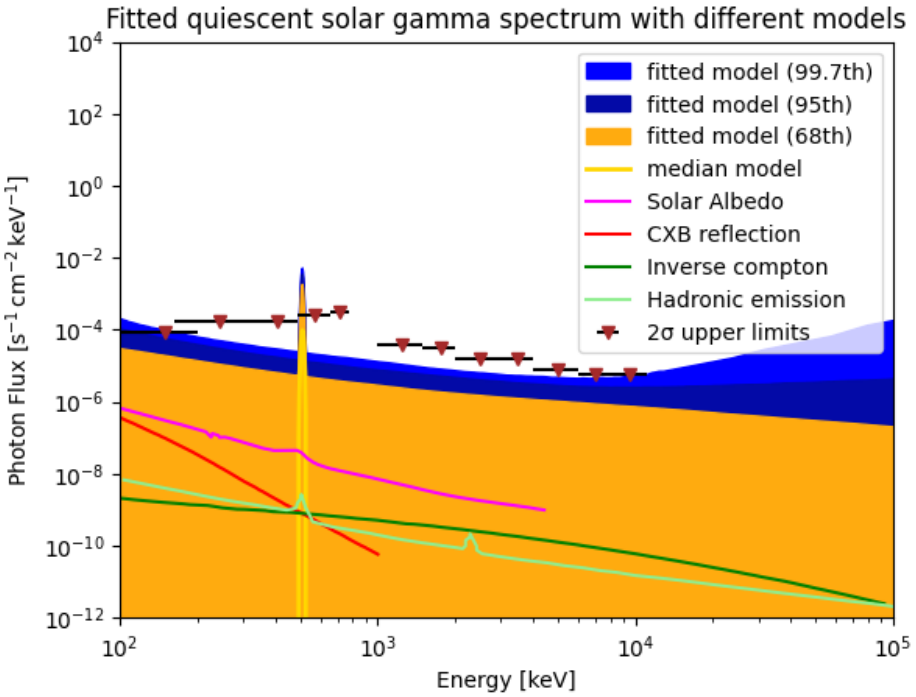

Figure 3.6.: Bayesian fit of the quiescent solar gamma-ray spectrum from Fig. 3.5 with different physical models. The expected solar albedo from Peterson et al. (1966), the reflected CXB emission from Churazov et al. (2008), the inverse compton radiation from Orlando et al. (2021) and the calculated hadronic emission from Mazziotta et al. (2020) is shown.

4. The Compton Spectrometer and Imager

The Compton Spectrometer and Imager (*COSI*) is a confirmed Small Explorer (*SMEX*) mission, which will observe the 'Mev-gap" of the gamma-ray sky. The launch is scheduled for 2027 and the mission is planned to last for 2 yr. The wide-field-of-view telescope operates in the $0.2 - 5\,\mathrm{MeV}$ energy range and maps the whole sky within one day. *COSI* is going to be in a low-earth orbit with an orbital period of about 100 min. Every 12 h the satellite changes its pointing from 22° North of zenith to 22° South of zenith and vice versa (Tomsick et al., 2019). Fig 4.1 shows that this alternation leads to an observation of the whole sky. *COSI* is based on a stacked array of 16 germanium cross-strip-detectors,

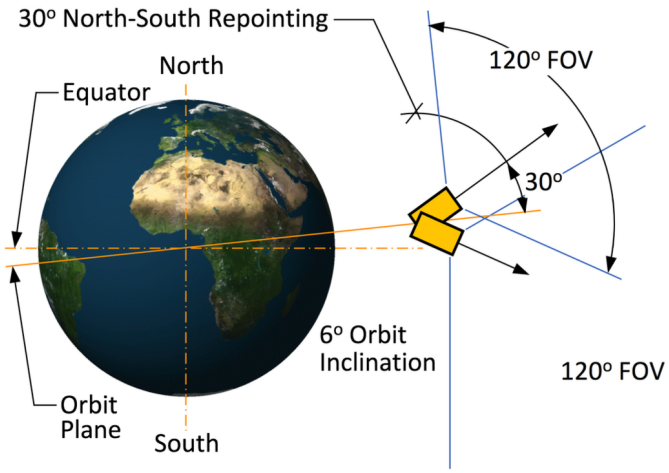

Figure 4.1.: The two different pointing orientation of *COSI* (yellow rectange) are shown. The Orbit inclination with respect to the Equator plan has been changed to go to a low-Earth orbit of less than 2° inclination. The north/south pointing has been adapted from ±30° to ±22°. With the $1\,\pi$ sr FOV, *COSI* maps the whole sky after the total change of 44° of the pointing zenith angle. Figure taken from (Tomsick et al., 2019).

which are housed in a cryostat and cryogenically cooled to below 80 K (Tomsick et al., 2019). The detectors are shielded on five sides by an active scintillator, which is made of bismuth germanium oxide (BGO). The field of view is defined by the shields to be 25% of the sky. Together with reducing background and detecting background radiation through anticoincidence, the shields expand *COSI*'s field of view for detecting GRBs to approximately 50% (Tomsick et al., 2019). The setup of *COSI* instrument is shown

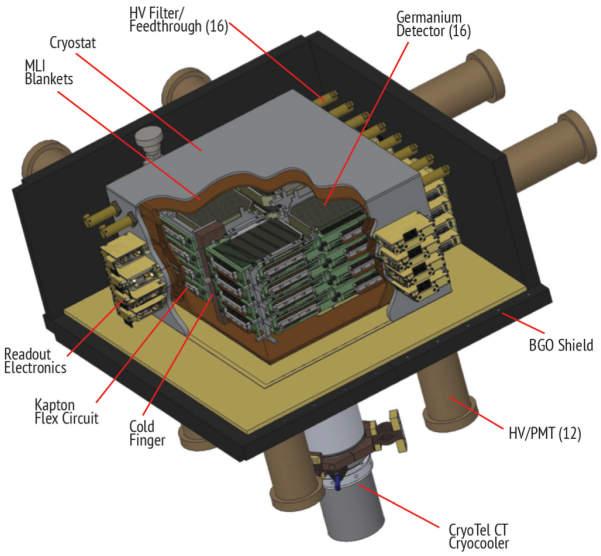

Figure 4.2.: The cutaway view of the COSI instrument shows 4×4 arranged germanium detectors and the used cyrostat, circuits, readout electronics and other components, surrounded by the BGO shield. Figure taken from (Tomsick et al., 2019).

in Fig 4.2. Compton telescopes utilizes compton scattering to detect incoming gamma-rays. The initial energy and the direction of an incoming photon is determined using the measurements of the emerging scattered electrons in the detector. The first scattered photon at position r_1 undergoes at least one more interaction at position r_2 within the detector. The measured energies of the incoming and scattered photons, combined with the direction $r_2 - r_1$, allow for narrowing down the direction of the incoming photon to a Compton cone, where the Compton angle serves as the cone's inclination, as shown in Figure 4.3. The intersection of the compton cones from further detected events from the same source reveal the position of the source.

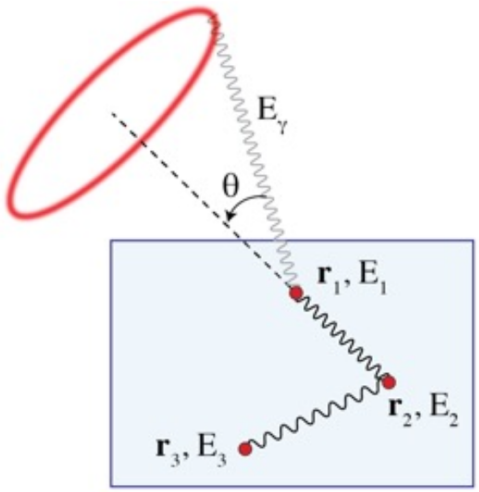

Figure 4.3.: Illustration of the interaction sequence of a single gamma-ray in a Compton telescope. Figure taken from (Tomsick et al., 2019).

4.1. Mission goals

4.1.1. Explore the origin of Galactic positrons

The dispersion and the annihilation of positrons in the Galactic ISM still remains uncertain. The precise mapping of the Galactic 511 keV line will reveal a possible substructure in the current model of the Galactic positron annihilation. The detection of individual sources or the determining of a truly diffuse emission and the precise measurement of the scale height of the disc emission are goals of this exploration. Furthermore the conditions in different Galactic regions where positron annihilation occurs will be probed. With a spectral resolution (FWHM) of 6.0 keV, an angular resolution (FWHM) of 4.1°, and a line sensitivity (3σ narrow line point source sensitivity in 2 yr of survey observations) of 1.2×10^{-5} photons cm^{-2} s^{-1} at 511 keV, *COSI* is best suited for these goals (Tomsick et al., 2023).

4.1.2. Revealing element formation

The energy range observed by *COSI* covers several nuclear emission lines. Elements such as ^{26}Al, ^{60}Fe and ^{44}Ti are predominantly produced in supernovae (SNe). The detection of the decay trace of these elements provide information about the star formation in the Galaxy over the past million years. For this mission, *COSI* features a line sensitivity of 3.0×10^{-6} photons cm^{-2} s^{-1} for the emission lines of these four elements (Tomsick et al., 2023).

4.1.3. Polarization measurements

The measurement of the polarisation of the detected gamma photons, enables the determination of emission mechanisms and source geometries. This kind of observation of gamma-ray bursts (GRB) provides information about the jet magnetic field structure, the jet composition, the energy dissipation process, and the emission mechanism (Tomsick et al., 2019).

4.1.4. Multimessenger astrophysics

With the capabilitiy to detect and localise short GRBs, *COSI* will significantly contribute to multimessenger astrophysics. Short GRBs are counterparts to sources of gravitational waves such as binary neutron stars mergers and to sources of high-energy neutrinos and will therefore help to localise them (Tomsick et al., 2019).

4.2. The positron puzzle

The measured distribution of the Galactic gamma-ray emission line at 511 keV (Fig. 1.1) raises the question of the origin and annihilation of Galactic positrons. The data show a strong concentration at the Galactic bulge, but also a significant disc emission. The bulge-to-disk luminosity ratio of ~ 1 is significantly higher than for any other astrophysical source distribution (Siegert, 2023). There are a lot of different sources for positrons which were considered to explain the amount and the distribution of the positron annihilation. Core-collapse supernovae and Type Ia supernovae enrich the interstellar medium (ISM) with certain isotopes ejected during the explosion. Ejected isotopes such as ^{26}Al, ^{44}Ti and ^{56}Ni can now produce positrons through β^+-decay. Estimation of the resulting annihilation rate by these elements alone cannot explain the measured Galactic 511 keV flux. Furthermore, the distribution of supernovae does not match the high bulge-to-disk ratio (Siegert, 2023). Compact objects such as microquasars and other X-ray binaries (XRBs) emit strong X-rays and are sources of relativistic jets. Positrons are produced by pair production through photon-photon interactions. These sources could explain the total annihilation rate, but it is still uncertain. Pulsars are also sources of positrons due to pair production in their magnetic fields. However, the bulge emission cannot be explained by the distribution of pulsars either. Flares and coronal mass ejections from stars release large quantities of particles, including positrons. The positrons are produced when accelerated particles collide with other particles, creating pions. These pions then decay to produce positrons. Stars as sources of the Galactic 511 keV flux are particularly interesting as a hypothesis because the Galactic stellar population already fits the 511 keV map quite well (Siegert, 2023).

The propagation of positrons through the Galaxy before they annihilate is important in explaining the difference between the sources and sinks of positrons. The measured positronium (Ps) fraction, which indicates how many positrons undergo the formation of Ps before they annihilate, is about $92 - 97\%$ (Siegert, 2023). This suggests that the annihilation takes place mainly in warm interstellar gas. This could explain the discrepancy between the distribution of potential positron sources and the distribution of the Galactic 511 keV emission.

5. Estimating the detectability of solar MeV emission with COSI

In order to assess how significant the Sun could be detected by *COSI*, we calculate how many solar photons will be detected compared to the instrumental background radiation that is constantly detected by *COSI* and the total Milky Way emission in the MeV range in different bands. For this, we calculate the signal to noise ratio S, given in units of standard deviations σ. We select 5σ as our detection limit in what follows. Since we are dealing with counting processes, we use Poisson statistics to describe the uncertainties of the measured photons, which gives $\sigma = \sqrt{N}$, where N is the number of counted events. Hence, we calculate the significance S as follows:

$$S[\sigma] = \frac{C_{Sun}}{\sqrt{C_{Sun} + C_{MW} + C_{IBG}}}, \tag{5.1}$$

where C_{Sun} being the total counts of photons from the Sun, C_{MW} being the total counts of photons from the diffuse Milky Way emission and C_{IBG} being the total counts of photons from *COSI*'s instrumental background. Since the number of the detected photons rises linearly with increasing observation time t, the significance rises proportional to $\sqrt{t}$. This method provides only a rough approximation of how the significance should be calculated. In Li et al. (1983), the likelihood function for an ON-OFF measurement, for example, is used to obtain the likelihood ratio test statistics, which is asymptotic to the significance. In this setting here, the number of photons detected during the entire mission can be considered large enough that this approximation is generally valid or slightly over-estimates the significance.
In the following sections, we will calculate how many photons are seen by *COSI* from different models of the quiescent solar gamma-ray emission, taking into account its rotating orientation, and estimate the significance.

5.1. Exposure map

The exposure map indicates the extent to which different regions of the sky are observed within a defined time and for different energy ranges. The units quantifying the exposure maps are $\mathrm{s} \cdot \mathrm{cm}^2$. The time component results from the duration a certain point in the

sky is observed, and the area component results from the effective detector area A_{eff} exposed to photons from a specific location in the sky. The exposure map is allocated at 10 different energy bins. Fig 5.1 shows the exposure map for an exposure time of 1 second for four different energy bins. The exposure map for energy bin 2 (=158 to 251 keV) shows the field of view to be about 25 % as mentioned in chapter 4. Furthermore, Fig. 5.1 shows that the higher the energy of the gamma radiation, the more permeable the shield becomes to this radiation, and *COSI* detects more radiation that does not come from the pointing direction.

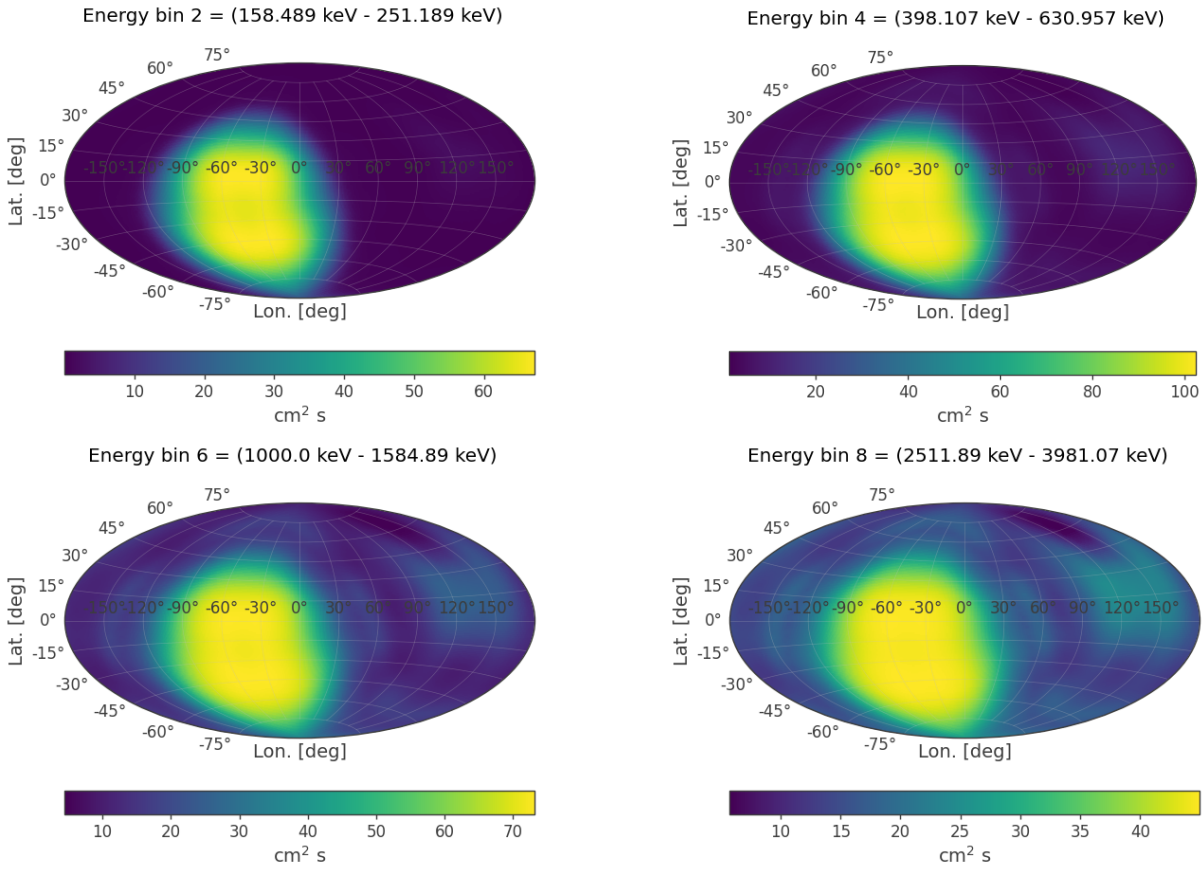

Figure 5.1.: Exposure maps in Galactic coordinates for an exposure time of 1 second for four different energy bins.

Fig. 5.2 shows the movement of *COSI*'s pointing direction during one orbit for an observation time of one minute. From the individual exposure maps for the various pointing directions, the exposure map for a whole orbit is now constructed, which contains the complete orientation of an orbit as shown in Fig. 5.3. The exposure map for the whole orbit from Fig 5.3 only shows one orbit with the 22° north-inclination. Therefore, the exposure map for one orbit with the 22° south-inclination is necessary to describe how the whole sky is observed. *COSI*'s orbit lies close to the ecliptic plane as visible in Fig. 5.3. The slight deviation from the ecliptic plane results from the inclination of the equatorial plane relative to the ecliptic plane of about 23° (Souami et al., 2012).

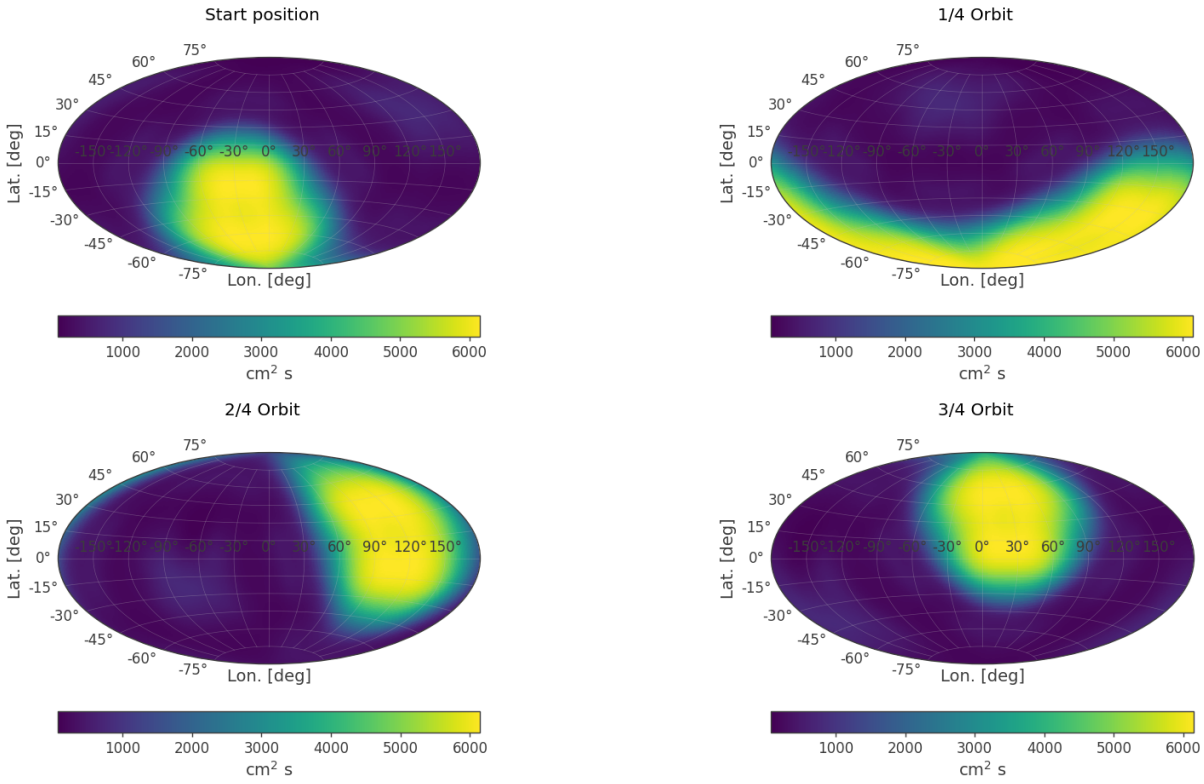

Figure 5.2.: Exposure map of the energy band 398 to 631 keV for four different pointing directions, equally distributed throughout one orbit and for one minute observation time.

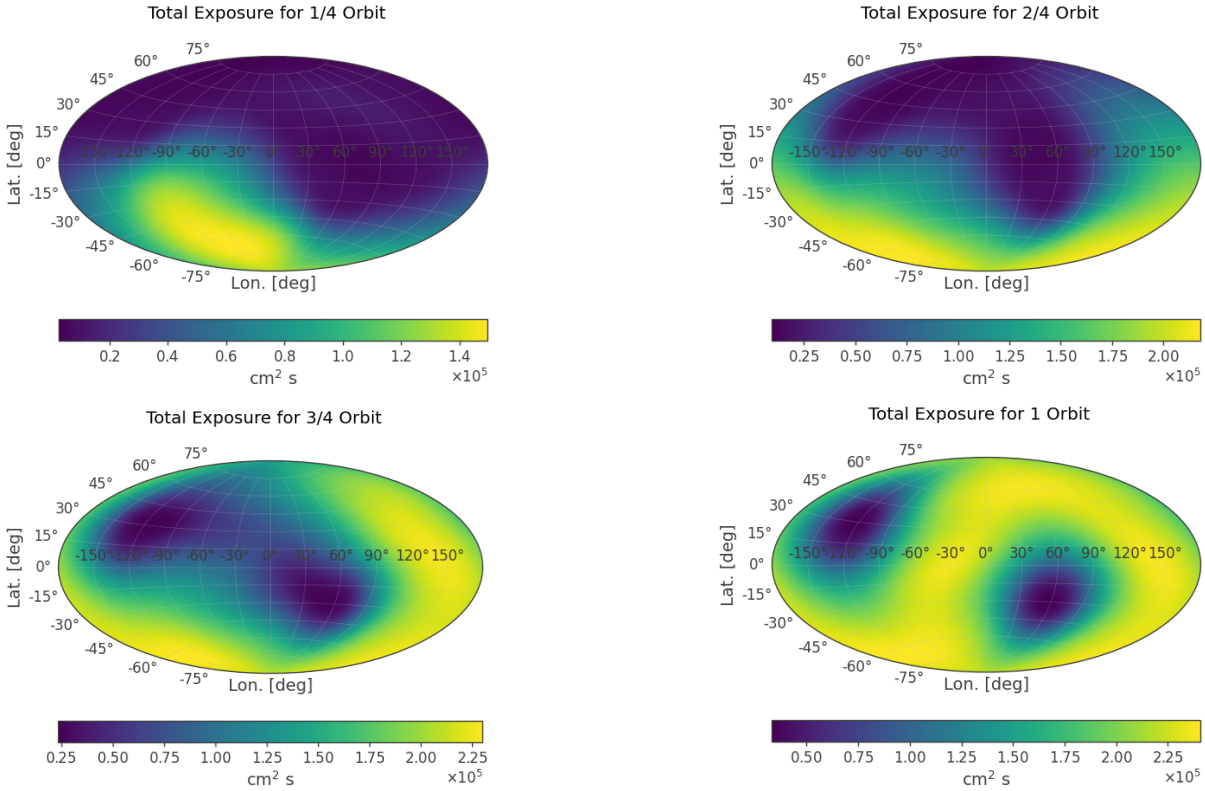

Figure 5.3.: Cumulative exposure map of the energy band 398 to 631 keV for 1/4, 2/4, 3/4 and a complete orbit.

5.2. Background radiation

5.2.1. Instrumental Background

The instrumental background arises mostly due to cosmic rays hitting the instrument. The incoming particles excite the material of the instrument through nuclear interactions, causing it to decay and emit photons, which end up as the instrumental background. The radiation causing these decays primarily originates from the particles shown in Fig. 2.7 and atmospheric neutrons. For the calculation of the significance, a simplified expected instrumental background from Karwin (2024) is used, which is shown in Fig. 5.4.

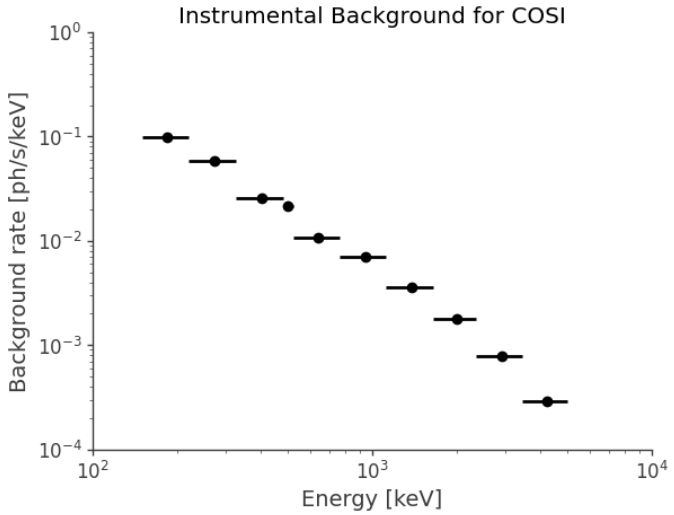

Figure 5.4.: *COSI*'s instrumental background subdivided into 10 energy bins from 150 keV to 5 MeV.

5.2.2. Milky Way Background

The positron annihilation in the Galaxy map from Siegert et al. (2016) (Fig. 5.5) is used as background radiation for the quiet Sun 511 keV emission model. 5.4. To take the diffuse gamma-ray background of the Milky Way for the continuum models into account, we use the model from Berteaud et al. (2022), which describes the INTEGRAL/SPI data of the diffuse Galactic gamma-rays. Although the spatial distribution of the diffuse emission differs slightly compared to the 511 keV emission (being dominated by the bulge rather than the disk), we will use this distribution as a surrogate to the actual distribution. (Fig. 5.5). Therefore, for the calculation of the significance for the different energy bins (which arise from the various energy bins from the exposure map and the instrumental background), we normalize the total flux of the positron annihilation map to the total flux of the diffuse background within the considered energy bin.

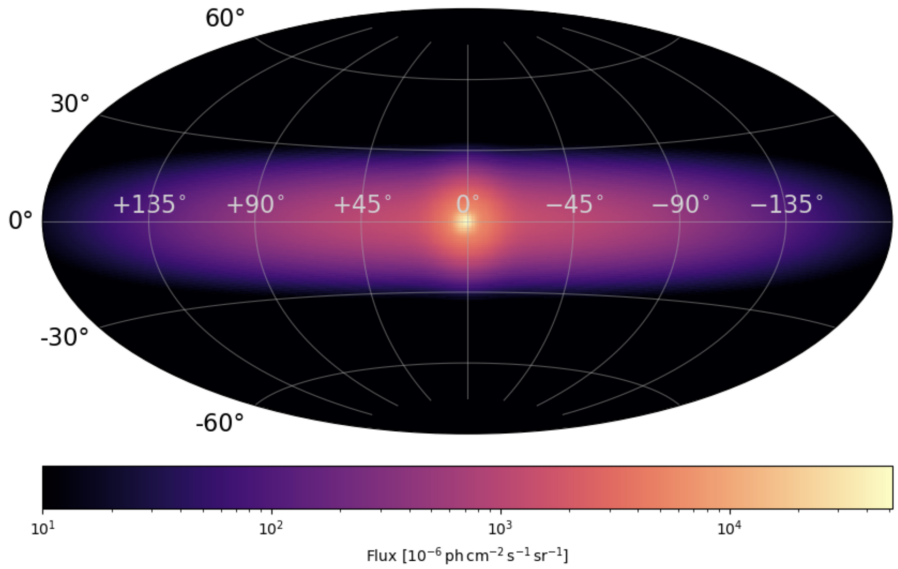

Figure 5.5.: Model of the positron annihilation in the Milky Way, from Siegert et al. (2016), which describes the data from INTEGRAL/SPI.

5.3. Position of the Sun

The exposure map shows that the position of an observed source is essential for the efficiency with which the emission from that source is detected. Since Earth orbits the Sun, the position of the Sun changes with respect to Earth throughout the year. Therefore, *COSI* observes a "moving" Sun. To determine the position of the Sun as observed from Earth over a period of two years, we utilized the `astroquery.jplhorizons`[1] module. The JPL Horizons online service offers access to essential solar system data and allows for the flexible generation of highly accurate ephemerides for solar system objects. The trajectory of the Sun as seen from *COSI* is shown in Fig. 5.6.

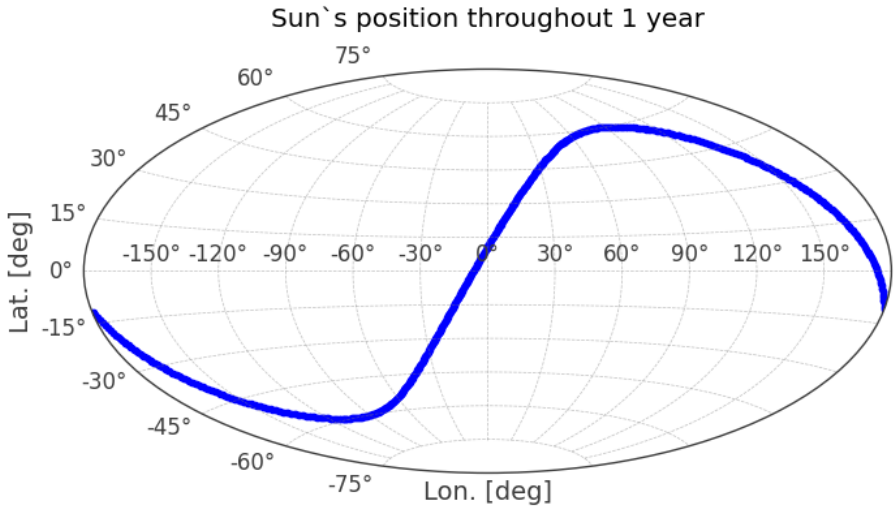

Figure 5.6.: Sun's trajectory throughout one year as seen from Earth.

[1] `https://astroquery.readthedocs.io/en/latest/jplhorizons/jplhorizons.html`

In order to model the Sun as an object being observed by COSI, we use a 2D Gaussian with a width of 0.5 deg centred on the path as shown in Fig. 5.6. This is then slightly larger as the disk of the Sun (diameter of 0.5 deg) and may take into account the extended Inverse Compton scattering among other processes that extend the apparent size of the Sun at MeV energies. Given that COSI has an angular resolution of a few degrees, the details of this choice are negligible.

5.4. Estimating the significance of the 511 keV emission from a moving Sun in COSI observations

5.4.1. Significance for one day

As stated at the beginning of this chapter, the significance for a source increases with the square root of the time t. However, this only holds true under the assumption that the number of detected photons remains constant in time. When examining the significance for short time intervals (e.g., 1 min), this no longer applies, as we have a changing exposure map (Fig. 5.2). Since we are primarily interested in the significance over an entire day due to the movement of the Sun, the direct $\sqrt{t}$ increase in significance is approximately valid again because the exposure maps for a single day already cover the entire sky and do hardly change for the following days. Nevertheless, analyzing short time intervals is useful to illustrate the changes in the exposure map within the northern and southern orbits and the correct build up of the significance within a day.
For the following calculations we use the 511 keV line as a test case. We use a line flux of $6.87 \times 10^{-4}\,\mathrm{s}^{-1}\,\mathrm{cm}^{-2}$ which is consistent with the upper limits from Frost et al. (1966) . Here, we use a single energy bin from 507 to 515 keV because 8 keV is the 3σ bin around the 511 keV line which results from the FWHM from section 4.1. Fig. 5.7 shows the instantaneous significance for one minute intervals, in- and decreasing during one orbit with north inclination and one with south inclination. It starts at a position of *COSI*, where the Sun is not in the field of view, and then gradually moves into view over time until it is in a "perfect" position at $t = 23$ min. After that, it moves out of the field of view again until $t = 105$ min. This process repeats for the second orbit with the south inclination (peak at $t = 126$). It is visible, that the second peak is broader and slightly higher. The different results from the inclination of *COSI*'s orbit relative to the ecliptic plane, since the Sun is slightly better in the field of view (closer to zenith) for north or south inclination depending on the Suns position. Therefore, in one half of the year, the northern inclination results in a slightly higher significance and in the other half of the year the southern inclination results in a slightly higher significance for observing the Sun. The buildup of the total significance for two orbits is shown in Fig. 5.8 and was calculated

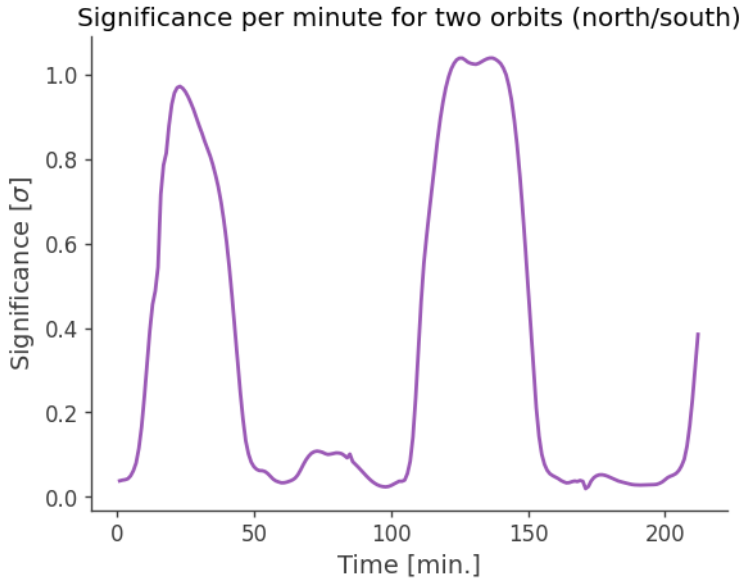

Figure 5.7.: Instantaneous significance values for 1 min time intervals for a total solar flux for the 511 keV emission of $6.87 \times 10^{-4}\,\mathrm{s}^{-1}\,\mathrm{cm}^{-2}$, where the Sun is located at $(\ell, b) = (186°, -29°)$. After about 100 min *COSI* slews to its south inclination.

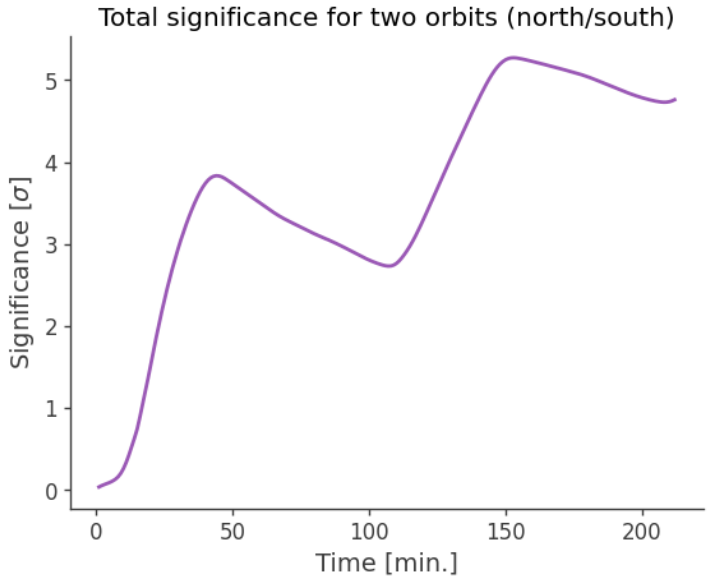

Figure 5.8.: Buildup of the total significance for one orbit with north inclination and one with south inclination.

as follows:

$$S[\sigma](t) = \frac{\sum_i^t C_{Sun,i}}{\sqrt{\sum_i^t C_{Sun,i} + C_{MW,i} + C_{IBG,i}}} \quad t \in [1, 212], \tag{5.2}$$

where $C_{Sun,i}$, $C_{MW,i}$, and $C_{IBG,i}$ are the Counts of the i-th one minute interval. Fig. 5.8 shows the gradual rise of the significance in which the $\sqrt{t}$ dependence isn't cognizable and the total significance even drops again after the two peaks. This is because when *COSI* is pointing away from the Sun, it still detects the background, which then makes the total counts less significant than at the last time *COSI* was pointing towards the Sun. The

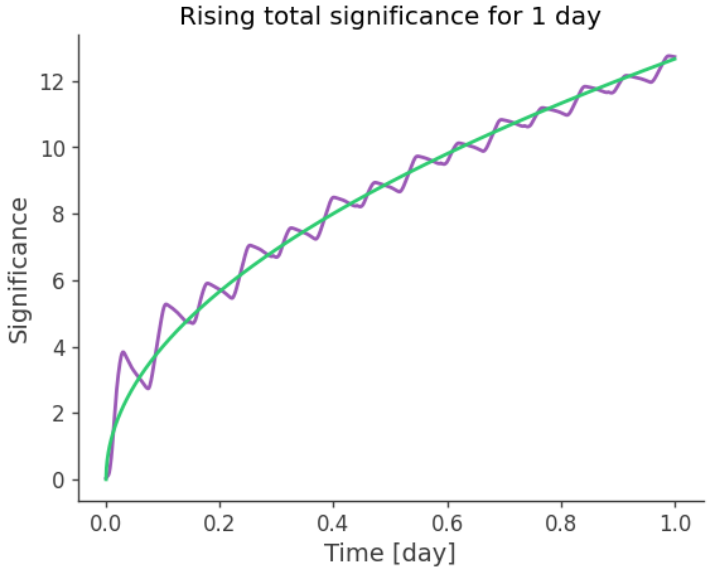

Figure 5.9.: The gradually rising total significance, calculated using the different exposure maps for one minute (purple) compared to the $\sqrt{t}$ rising of the total significance calculated using the exposure map for one day (green).

total significance for a whole day shows a gradually increase that now clearly builds up the $\sqrt{t}$ increase (Fig. 5.9). The direct $\sqrt{t}$ increase is determined by the exposure map for an entire day, which includes the complete sky observation. As expected, the long-term trend gives the same results, but may be more significant for smaller time intervals. The gradual increase thus demonstrates the correct rise in significance for one day.

5.4.2. Significance for two years

Because COSI's angular resolution is 4.1° at 511 keV, we can treat the Sun as a stationary source for one day. In a subsequent day, we then shift the Sun by $360°/365.25 = 0.986°$ to its next position along its trajectory. The significance for the different days within one year, and thus for the different positions, is shown in Fig. 5.10. As expected, it exhibits a maximum significance at two days. At these days, the Sun is located where the ecliptic plane intersects with *COSI*'s orbital plane.

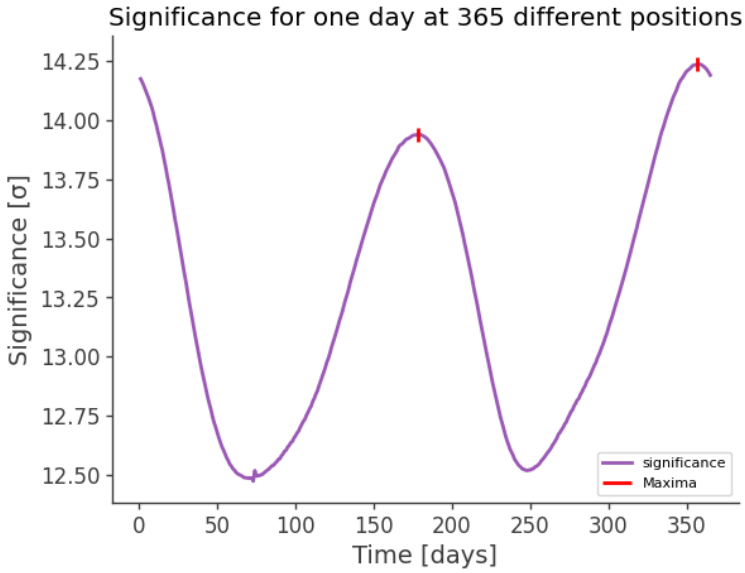

Figure 5.10.: instantaneous significance values for one day time intervals throughout one year. Every day the Sun is located at a different position. The two position of the maxima are about (ℓ, b) = (-87°, 60°) at day 179 and (ℓ, b) = (94°, -60°) at day 358.

Having determined the significance for one day at each position, we calculate the cumulative significance over two years and examine flux at which we consider it significant. Fig 5.11 shows the significance for the 2 yr observation time for different fluxes. Up to a value of $\sim 10^{-2}\,\mathrm{photons\,s^{-1}\,cm^{-2}}$, the significance increases linearly with rising flux. At this level, the background $C_{MW} + C_{IBG}$ dominates the square root term in (5.1) resulting in $S \sim C_{Sun}$. Beyond this range, the graph changes slope as the counts from the Sun begin to significantly influence the square root term. After this "transition region", the number of photons from the Sun will dominate the square root term, and the graph will stagnate with a slope of 1/2, reflecting the behavior of the significance $S \sim \sqrt{C_{Sun}}$. The flux at which a significance $S > 5\sigma$ is achieved is $\sim 9.16 \times 10^{-6}\,\mathrm{photons\,s^{-1}\,cm^{-2}}$, as shown in Fig. 5.11. This results in a new 3σ narrow line point source sensitivity for a 2 years observation time of $\sim 5.5 \times 10^{-6}\,\mathrm{photons\,s^{-1}\,cm^{-2}}$, which is about half the value reported in Tomsick et al. (2023), thus improving the sensitivity for an observation of the Sun.
To get a better comparison of this calculation with the sensitivity of *COSI* from Tomsick et al. (2023) ($1.2 \times 10^{-5}\,\mathrm{photons\,cm^{-2}\,s^{-1}}$) we treat the Sun as a stationary source and place it at different positions across the sky (see a more detailed description in section 5.6). The flux required to obtain a significance of $S = 3\sigma$ for an observation time of 2 yr at the least observed position in the sky is $1.05 \times 10^{-5}\,\mathrm{photons\,s^{-1}\,cm^{-2}}$. This value gives an upper limit to the line sensitivity for the 511 keV flux. It is close to the value from Tomsick et al. (2023), but improves it a little bit. The mean value of the 3σ line sensitivity over the whole sky is $\sim 6.45 \times 10^{-6}\,\mathrm{photons\,s^{-1}\,cm^{-2}}$.

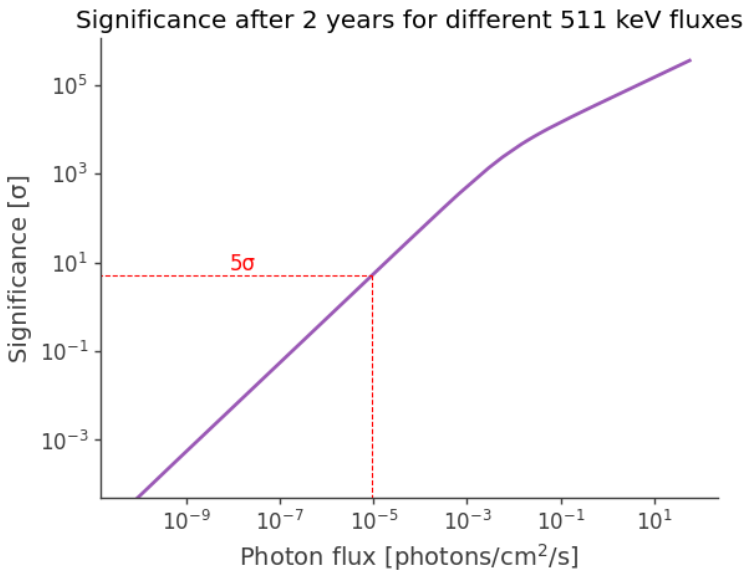

Figure 5.11.: Significance of the solar 511 keV flux after 2 yr observation time as a function of the flux. The flux $\sim 9.16 \times 10^{-6}\,\mathrm{photons\,s^{-1}\,cm^{-2}}$ at which $S \geq 5\sigma$ is marked.

5.5. MeV Continuum Significance Estimates

5.5.1. Significance for two years

Analogous to section 5.4.2, we calculate the significance for 2 years observation time for the different continuum energy bins. As mentioned in section 5.2, these energy bins are defined by the boundaries of the exposure maps and the instrumental background, resulting in 18 energy bins. The significance for the whole energy range was calculated as follows:

$$S[\sigma](N_E) = \sqrt{\sum_{i}^{N_E} S_i^2} \quad N_E \in [1, 18], \tag{5.3}$$

where S_i is the significance of the flux within the i-th energy bin. Fig. 5.12 shows the significance as a function of the power-law amplitude a and the power-law index b. Analogous to Fig. 5.11, the figure on the left shows a linear increase in significance, with the amplitude not becoming large enough to reach the "transition region", resulting in no change in slope. The figure on the right shows a parabolic dependence of significance on the power-law index b. The minimum significance occurs at a power-law index of $b = -1.38$. The first decreasing and then increasing significance is due to the fact that, for indices $b > -1.38$, the decrease in significance due to the decreasing flux below 1000 keV is offset by the increasing flux above 1000 keV.
The significance for different configurations of a and b is shown in Fig. 5.13. The parabolic dependence of the significance on b is visible and since the amplitude a remains in the

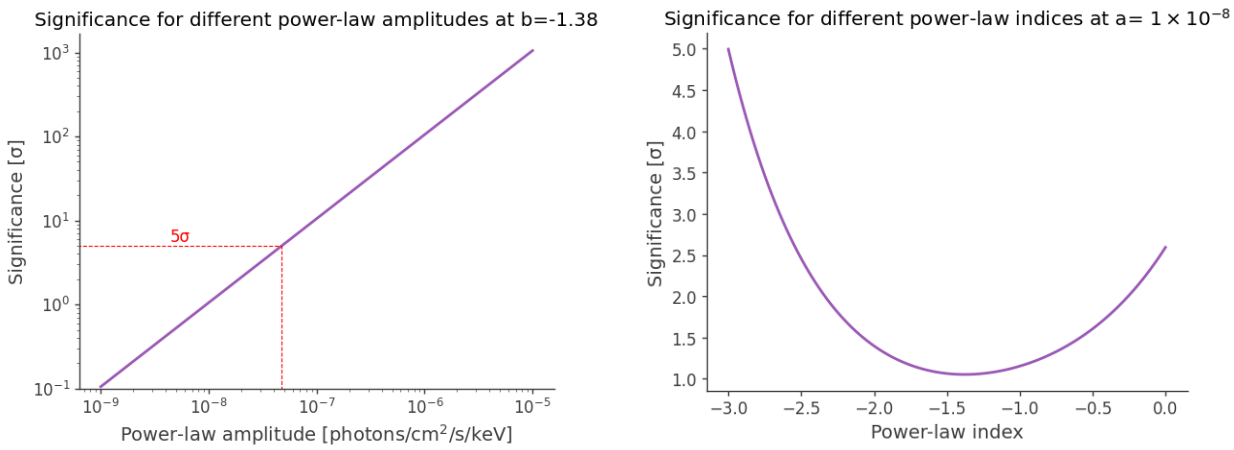

Figure 5.12.: Significance of the continuous solar flux after 2 years of observation as a function of the power-law amplitude a at constant $b = -1.38$ (left) and as a function of the power-law index b at constant $a = 1e - 8$ (right). The power-law amplitude ($4.75 \times 10^{-8}\,\mathrm{photons\,s^{-1}\,cm^{-2}\,keV^{-1}}$), which gives a significance of $S = 5\sigma$ at an power-law index of $b = -1.38$, is marked.

linear region, the distribution of the significance remains the same across the three figures, each differing by a factor of 10. Significances of 5σ are highlighted, showing that above an amplitude of about $a = 4.75 \times 10^{-8}\,\mathrm{photons\,s^{-1}\,cm^{-2}\,keV^{-1}}$ the power-law index no longer affects whether the measured flux reaches a significance $> 5\sigma$.

5.6. Significance of a stationary source

Since we are dealing with a moving source, it is useful to know how the significance of the same source would change if it were stationary. For this evaluation we use the power-law model for the continuum with an amplitude of $a = 9.0 \times 10^{-6}\,\mathrm{photons\,s^{-1}\,cm^{-2}\,keV^{-1}}$ and an index of $b = -0.8$, which is the mean index from Fig. 3.4. The calculated significance for a stationary source at different positions in the sky is shown in Fig. 5.14. The figure reproduces the exposure map, as regions that are more efficiently observed lead to higher significance. The power-law index therefore affects the appearance of this distribution, as the exposure maps differ at different energy regions (see Fig. 5.1) and the index determines the strength of the flux in these regions.

Comparing these significances with those of the measured flux from the moving Sun using the same power-law model shows that about 24% of the sky would exhibit higher significance if a stationary source was located there. Fig. 5.15 shows the positions which have a higher significance. The trajectory of the Sun illustrates its passage through regions of higher and lower significance, ultimately leading to the effective significance of $S = 1125\sigma$ after 2 yr.

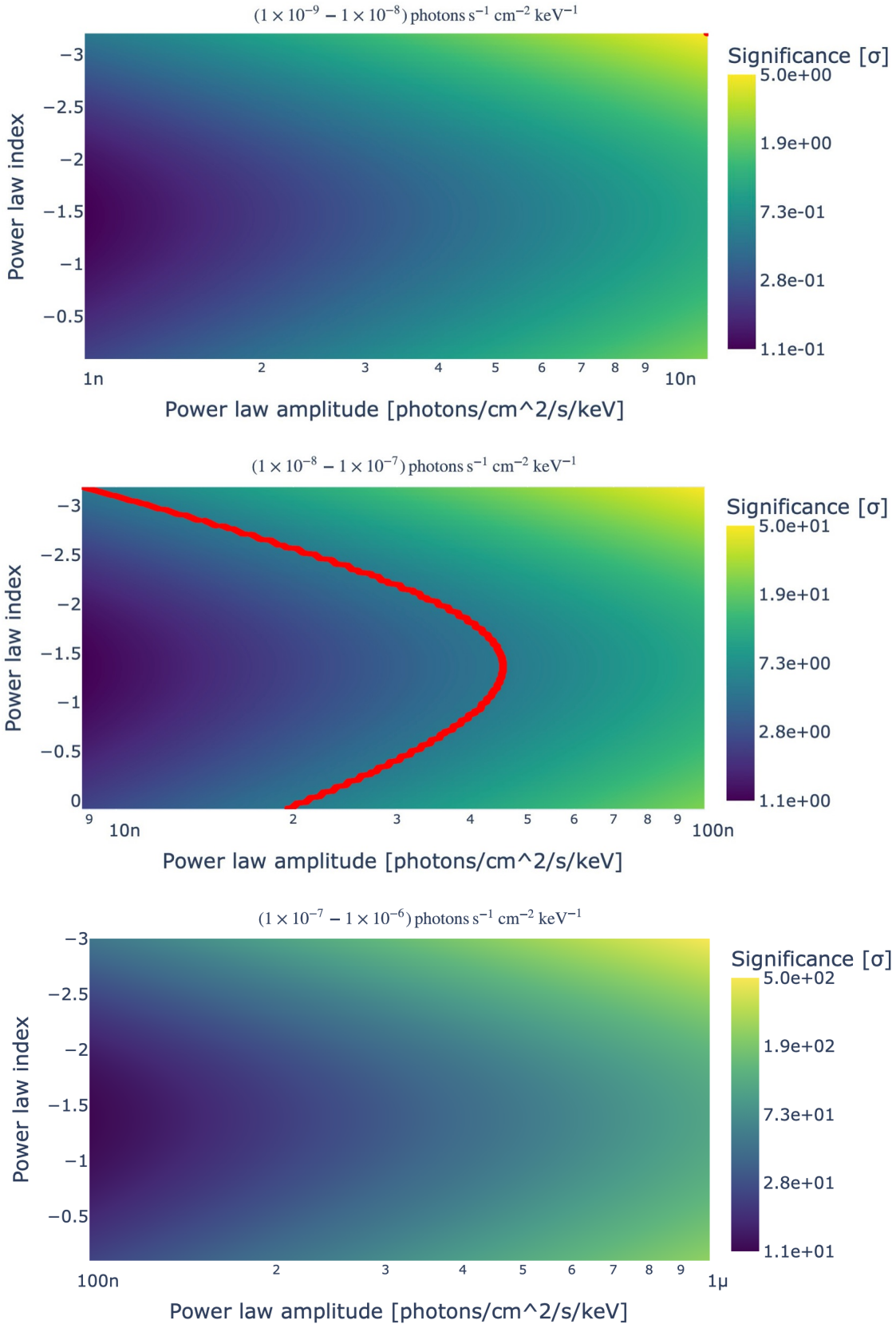

Figure 5.13.: Significance of the continuous solar flux after the 2 yr of observation as a function of the power-law index b and the power-law amplitude a for three different amplitude ranges. The configurations leading to a significance of 5σ are highlighted in red.

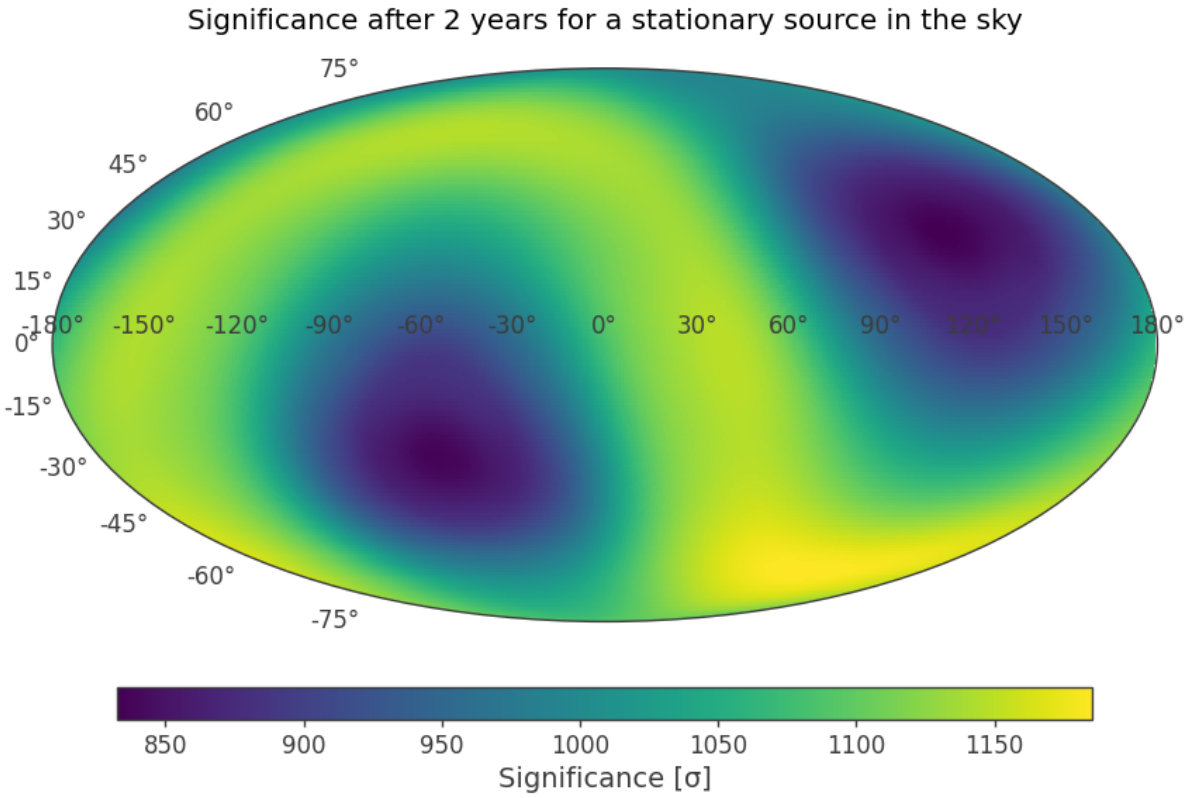

Figure 5.14.: Map of the whole sky showing the 2 yr significance for stationary sources with the continuous flux 3.2×10^{-2} photons s^{-1} cm^{-2} within 150–5000 keV.

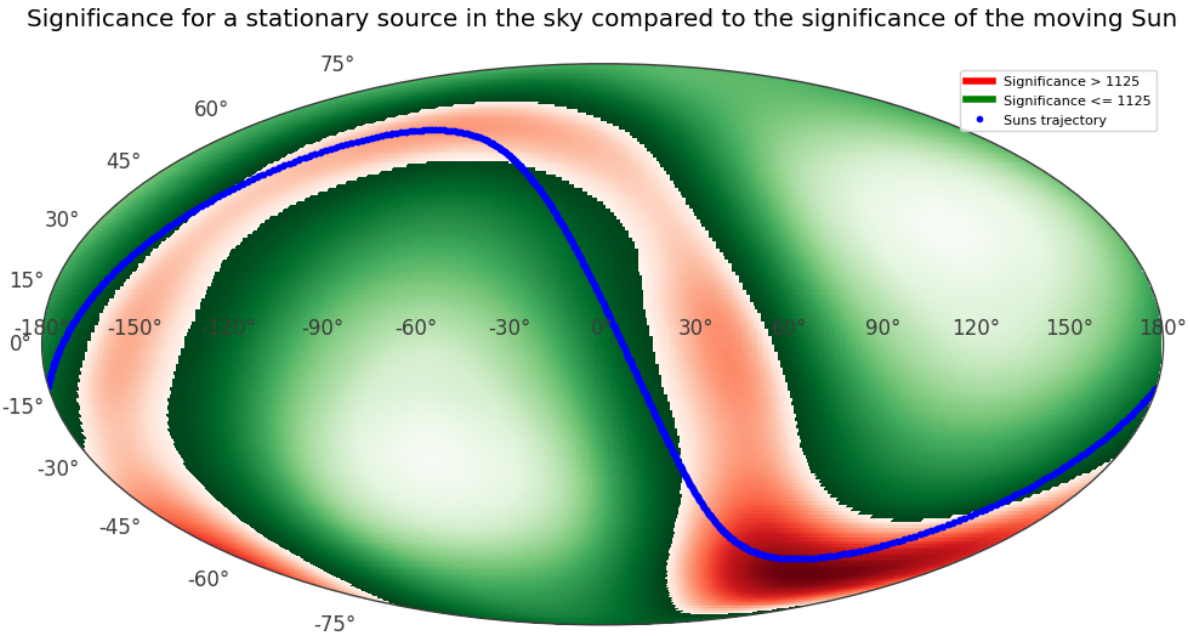

Figure 5.15.: The regions of the sky with a stationary significance less than the significance of the moving Sun (1125σ), with the continuous flux 3.2×10^{-2} photons s^{-1} cm^{-2} within 150–5000 keV, are highlighted in green, and the regions with a higher significance are highlighted in red. The trajectory of the Sun is also shown for comparison.

5.7. Detectability of the Sun in the MeV range from astrophysical modelling

Since the Peterson solar albedo model (Peterson et al., 1966) predicts the highest quiescent solar flux, this is the physical model that we will examine in the following. To extract the solar flux we fit a broken power-law to the model:

$$\text{Broken power-law} \begin{cases} A\, x^{-\alpha_1} & \text{for } x < x_{break}, \\ A\, x_{break}^{\alpha_2-\alpha_1}\, x^{-\alpha_2} & \text{for } x \geq x_{break}. \end{cases} \tag{5.4}$$

Where A is the amplitude, α_1/α_2 are the two power-law indices, and x_{break} is the break energy. The following values were obtained from the fit:

$$A = 5.91 \cdot 10^{-3},\ \alpha_1 = 1.97,\ \alpha_2 = 1.3,\ x_{break} = 1273\,\text{keV} \tag{5.5}$$

The significance resulting from this spectrum is shown in Fig. 5.16.

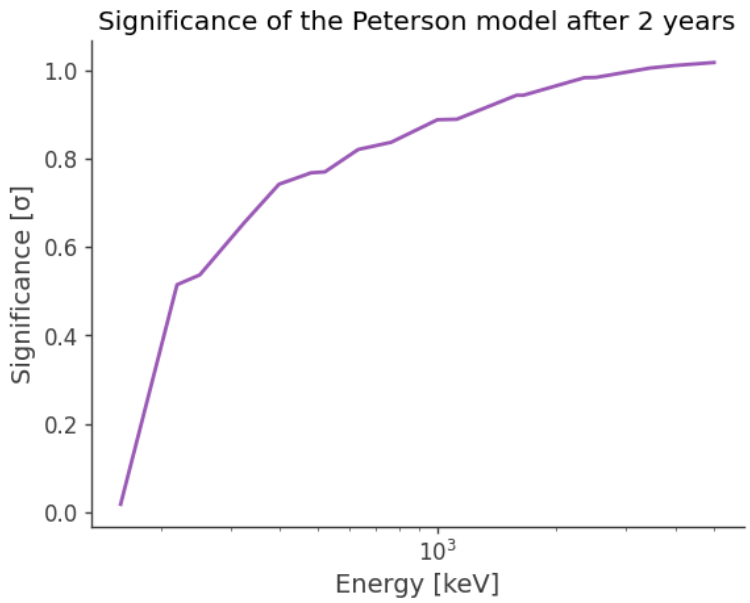

Figure 5.16.: Growing significance after 2 yr of the Peterson model with the continuous flux 4.68×10^{-5} photons $\text{s}^{-1}\,\text{cm}^{-2}$ over the energy range (150-5000 keV).

After two years, a significance of about 1σ is reached. Consequently, to reach 5σ, an observation time of 50 years is required.

$$t_{5\sigma} = \left(\frac{5\sigma}{S_{1\text{yr}}[\sigma]}\right)^2 = \left(\frac{5\sigma\sqrt{2\text{yr}}}{S_{2\text{yr}}[\sigma]}\right)^2 = \left(\frac{5\sigma}{1\sigma}\right)^2 \cdot 2\text{yr} = 50\,\text{yr}, \tag{5.6}$$

where $S_{1\text{yr}}/S_{2\text{yr}}$ is the significance after one/two years. Analogously, an observation time $t_{3\sigma}$ of 18 yr is required to achieve a significance of 3σ. Fig. 5.16 shows that due to the

profile of the spectrum (Fig. 2.10), the significance is mainly built up by the spectrum in the range below $< 1\,\mathrm{MeV}$.
The obtained significance of 1σ is consistent with *COSI*'s continuum sensitivity reported in Tomsick et al. (2023). Fig. 2.10 shows, that the 1σ continuum sensitivity (1/3 of the 3σ continuum sensitivity) begins to intersect with the Peterson spectrum.

6. Simulations for the Compton Spectrometer and Imager

We will now use the astrophysical model from Peterson et al. (1966) to perform particle-by-particle Monte-Carlo simulations with GEANT4-based `MEGAlib`[1] ((Allison et al., 2006), (Zoglauer et al., 2006)). For this simulation we use the *COSI-SMEX* massmodel shown in Fig. 6.1. It provides details of the detectors, how they are configured, the resulting sensitivity and other aspects affected by the various components of the satellite. The

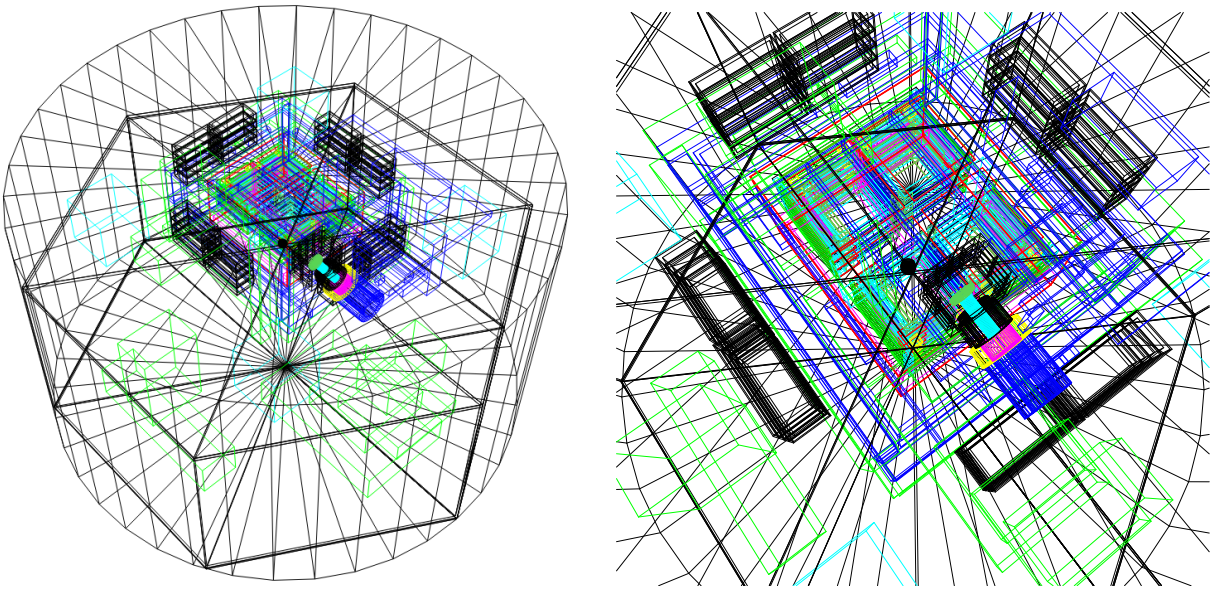

Figure 6.1.: Massmodel for the *COSI-SMEX* instrument with cylindrical satellite bus. The instruments are colored. The stacked 4×4 arranged germanium detectors are shown as green rectangles in the zoom in.

simulations are conducted within the `COSItools`[2] software package and proceed as follows: `Cosima`[2] simulates the detector response to the gamma-ray sources; `Revan`[2] performs the Compton or pair event reconstruction of the simulations; and `Mimrec`[2] enables image reconstruction and higher level analysis. For the simulation with `Cosima`[2], a source file is needed. It provides information about the spectrum and location of the source and about the orientation of *COSI*. The file also contains information about the Earth's shielding

[1] `https://megalibtoolkit.com/home.html`
[2] `https://github.com/zoglauer/COSIpy`

of the source. For this simulation, we use the broken power-law from section 5.7 , with $A = 5.91 \times 10^{-3}$, $\alpha_1 = 1.97$, $\alpha_2 = 1.3$, $x_{break} = 1273\,\mathrm{keV}$ within the energy range (150–5000 keV), which gives a flux of $4.68 \times 10^{-5}\,\mathrm{photons\,s^{-1}\,cm^{-2}}$. Similar to the 2 yr significance calculation, we run the simulations on a daily basis. For each day and its corresponding position, a source file was generated. All source files use the same gamma-ray flux, and the Sun is treated as a far-field point source. The orientation file for *COSI*, which contains its pointing direction, was divided into daily segments and distributed across the different source files. For each source file, a simulation was initiated using `Cosima`[2] and `Revan`[2]. The resulting .tra files, which contain the simulation results from `Revan`[2], were then combined into a single file, enabling the image and energy spectrum reconstruction for the entire image of the moving Sun.

The simulation for 2 years resulted in 208,074 generated and analysed events, of which 72,924 could be reconstructed. The detected events were mostly discarded because an unwanted photoeffect event occurred. The reconstructed spectrum from these events is shown in Fig. 6.2. Since we are simulating a continuous flux, logarithmic binning is used to create the energy spectrum. Fig. 6.2 also shows that the shape of the reconstructed spectrum reflects the shape of the initial spectrum.

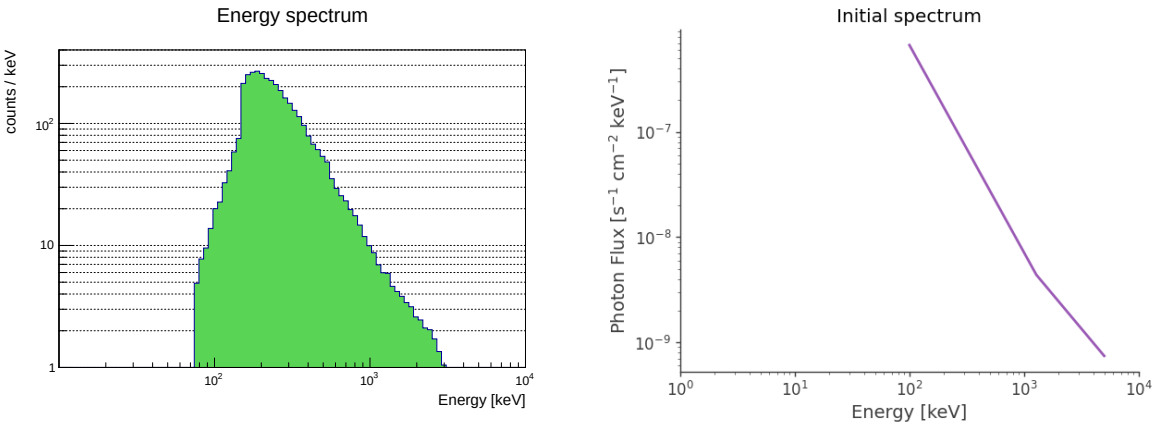

Figure 6.2.: Energy spectrum for 2 yr observation after reconstruction for the whole instrument (left). Initial spectrum from Peterson et al. (1966) used for the simulations (right).

Fig. 6.3 shows the image reconstruction of the Sun for one day at four different positions. Since we don't include any background, the reconstruction works for one day and the Sun is clearly visible. The image reconstruction for 2 years of observation (Fig. 6.4) reveals Sun's trajectory throughout 2 years across the sky. Different regions with a higher detected flux (red spots) due to *COSI*'s orientation are visible. These mostly occurs when the Suns trajectory overlap with the Galactic disc. This red spots do not align with the calculations above, since we would mostly expect two regions with higher detected flux around $(\ell, b) = (-87°, 60°)$ and $(\ell, b) = (94°, -60°)$.

It is important to treat the Sun as a moving source and not as a stationary source creating the image (Fig. 6.4) in two years. The Sun's radiation only comes from a specific directions at specific time. As these positions are observed with different sensitivities, this must be taken into account.

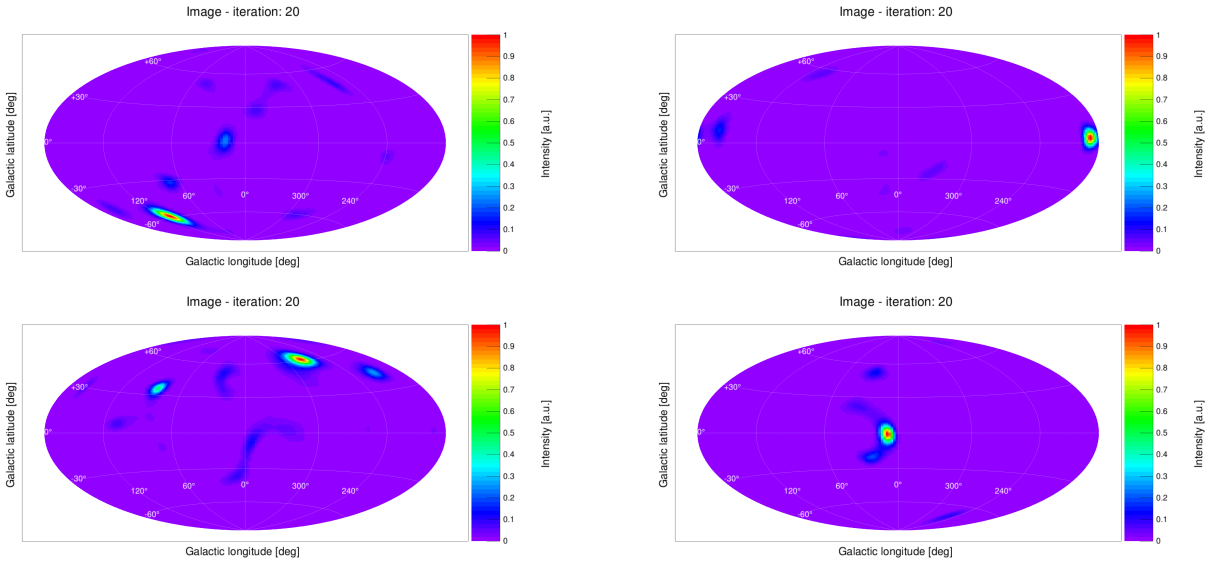

Figure 6.3.: Image reconstruction of the Sun for one day at four different positions using the astrophysical model from Peterson et al. (1966) for the energy range 150–5000 keV. No background is included. The Sun was placed at $(\ell, b) = (110°, -60°)$, $(\ell, b) = (-172°, 2°)$, $(\ell, b) = (-84°, 60°)$, $(\ell, b) = (6°, 0.5°)$.

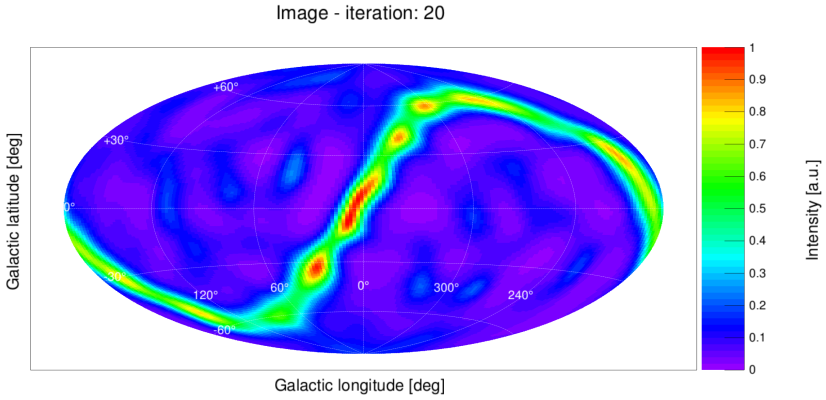

Figure 6.4.: Image reconstruction of the Sun for 2 yr of observation using the astrophysical model from Peterson et al. (1966) for the energy range 150–5000 keV. No background is included. The red spots show areas which are observed the most efficient.

7. Discussion & Conclusion

In this Thesis the gamma-ray emission from the quiet Sun was examined and estimated how significant this emission could be detected by the Compton Spectrometer and Imager (*COSI*). Previous measurements resulted in upper limits of the solar gamma-ray flux from 3 keV to 11 Mev, which are many orders of magnitudes above astrophysical expectations. These upper limits were used to establish different models of this flux with different likelihoods. A power-law model for the continuous flux and a gaussian model for the 511 keV line flux were analyzed. The fit to the upper limits resulted in the mean values $a = (0 \pm 3) \times 10^{-6}\,\mathrm{s^{-1}\,cm^{-2}\,keV^{-1}}$ for the power-law amplitude, $b = -0.79 \pm 0.64$ for the power-law index, and $c = (0.1 \pm 2.2) \times 10^{-2}\,\mathrm{s^{-1}\,cm^{-2}\,keV^{-1}}$ for the gaussian amplitude. To estimate how significant the flux could be detected by *COSI*, I utilized a signal to noise ratio approximation. The background radiation, which was included in this calculation, was the instrumental background and the Galactic gamma-ray emission. To estimate how many counts will be detected from a source at a specific location in the sky, I used *COSI*'s exposure map, which indicates the extent to which those regions are observed. Since the Sun is observed as a "moving" source, the counts within one day for one stationary position of the Sun were calculated. This was repeated for the Sun at 365 different Positions equally distributed throughout a year. This resulted in a maximum significance at two positions: (ℓ, b) = (-87°, 60°) and (ℓ, b) = (94°, -60°). The significance determined on a day-by-day basis was then used to calculate the significance for *COSI*'s planned observation duration of 2 yr. A 511 keV line flux of $\sim 5.5 \times 10^{-6}\,\mathrm{photons\,s^{-1}\,cm^{-2}}$ exhibits a significance of 3σ within 2 yr, resulting in an improved sensitivity for an observation of the solar 511 keV line flux compared to that reported in Tomsick et al. (2023) ($1.2 \times 10^{-5}\,\mathrm{s^{-1}\,photons\,cm^{-2}}$). The Sun as a moving MeV source is on average stronger than a stationary source in the sky. About 24% of the sky would exhibit higher significance than the Sun for a flux between 150–5000 keV. The calculated upper limit of the 3σ sensitivity for an observation time of 2 yr for a stationary source in the sky is $1.05 \times 10^{-5}\,\mathrm{photons\,s^{-1}\,cm^{-2}}$, which improves the value reported in Tomsick et al. (2023). The astrophysical model of the gamma-ray continuous flux from the quiet Sun from Peterson et al. (1966), resulted in a significance of $\sim 1\sigma$ for the 2 yr observation time. Therefore it would take 18 yr of observation to achieve a significance of 3σ. For the planned mission duration, it would therefore not be possible to measure such a flux with significant confidence. Whether *COSI*'s operational period will be extended long enough to detect

this flux remains uncertain at this time. However, the *COSI* mission will undoubtedly establish new upper limits of the solar gamma-ray flux within 150–5000 keV, which will increasingly constrain astrophysical models.

The 511 keV flux, which exhibit a 2 yr significance of 3σ is smaller than the quasi-persistent flux from the flaring Sun at 511 keV of $1.8 \times 10^{-4}\,\mathrm{photons\,s^{-1}\,cm^{-2}}$ (Mittal et al., 2024, in prep.). Adding the quiet Sun 511 keV contribution to the quasi-persistent flare flux would increase the stellar contribution to the Galactic 511 keV line by $\sim 3\%$. Since the stellar flare scenario can probably not explain large parts of the Galactic positron annihilation emission, adding 3% will not change this result. While the Sun might be a varying source for *COSI* in terms of continuum and 511 keV emission, the Galactic 511 keV emission is probably unaffected by the contribution of main sequence stars.

Bibliography

Abdo, Abdo, M. Ackermann, M. Ajello, L. Baldini, J. Ballet, Guido Barbiellini, Denis Bastieri, Keith Bechtol, Ronaldo Bellazzini, Bijan Berenji, Emanuele Bonamente, A. Borgland, Aurelien Bouvier, J. Bregeon, A. Brez, Michela Brigida, P. Bruel, R. Buehler, and Stefano Buson (Apr. 2011). "Fermi large area telescope observations of two gamma-ray emission components from the quiescent sun". In: *Astrophysical Journal* 734. DOI: 10.1088/0004-637X/734/2/116.

Allison, J., K. Amako, John Apostolakis, H. Araujo, Pedro Arce, Makoto Asai, Guy Barrand, Riccardo Capra, Stephane Chauvie, Radovan Chytracek, Pablo Cirrone, G. Cooperman, Gabriele Cosmo, Giacomo Cuttone, Giuseppe Daquino, M. Donszelmann, M. Dressel, G. Folger, Franca Foppiano, and H. Yoshida (Feb. 2006). "Geant4 Developments and Applications". In: *IEEE Transactions on Nuclear Science* 53, pp. 270–278. DOI: 10.1109/TNS.2006.869826.

Berteaud, J., F. Calore, J. Iguaz, P. D. Serpico, and Thomas Siegert (July 2022). "Strong constraints on primordial black hole dark matter from 16 years of INTEGRAL/SPI observations". In: *Physical Review D* 106. DOI: 10.1103/PhysRevD.106.023030.

Bishop, Christopher (Oct. 2007). *Pattern Recognition and Machine Learning (Information Science and Statistics)*. ISBN: 0387310738.

Churazov, E., S. Sazonov, Rashid Sunyaev, and M. Revnivtsev (Apr. 2008). "Earth X-ray albedo for cosmic X-ray background radiation in the 1-1000 keV band". In: *Monthly Notices of The Royal Astronomical Society - MON NOTIC ROY ASTRON SOC* 385, pp. 719–727. DOI: 10.1111/j.1365-2966.2008.12918.x.

Frost, K., E. Rothe, and Laurence Peterson (Sept. 1966). "A Search for the Quiet-Time Solar Gamma Rays from Ballon Altitudes". In: *Journal of Geophysical Research* 71. DOI: 10.1029/JZ071i017p04079.

Gruber, D., J. Matteson, L. Peterson, and G. Jung (Mar. 1999). "The Spectrum of Diffuse Cosmic Hard X-Rays Measured with HEAO1". In: *The Astrophysical Journal* 520. DOI: 10.1086/307450.

Hannah, I. G., G. J. Hurford, H. S. Hudson, R. P. Lin, and K. van Bibber (2007). "First Limits on the 3–200 keV X-ray Spectrum of the Quiet Sun Using RHESSI". In: *The Astrophysical Journal Letters* 659, L77–L80.

Hathaway, D. (2022). *The Solar Interior*. Accessed: 31.03.2024. URL: https://solarscience.msfc.nasa.gov/interior.shtml.

Karwin, Chris (2024). *cosi-data-challenge-2/backgrounds/README.md at main · cositools/cosi-data-challenge-2*. Accessed: 01.08.2024. URL: https://github.com/cositools/cosi-data-challenge-2/blob/main/backgrounds/README.md.

Krummheuer, B. (2019). *Max-Planck-Gesellschaft: Die langen Finger der Sonne*. Accessed: 17.04.2024. URL: https://www.mpg.de/14135295/die-langen-finger-der-sonne.

Li, Ti-Pei and YuQian Ma (Aug. 1983). "Analysis methods for results in gamma-ray astronomy". In: *The Astrophysical Journal* 272, pp. 317–324. DOI: 10.1086/161295.

Mazziotta, M. N., P. De la Torre Luque, L. Di Venere, A. Fass'o, A. Ferrari, F. Loparco, P. R. Sala, and D. Serini (Apr. 2020). "Cosmic-ray interactions with the Sun using the fluka code". In: *Physical Review D* 101. DOI: 10.1103/PhysRevD.101.083011.

Morton, R., Rahul Sharma, E. Tajfirouzhe, and Hemanthi Miriyala (Aug. 2022). *Alfvénic waves in the inhomogeneous solar atmosphere*. DOI: 10.48550/arXiv.2208.05222.

Orlando, E. and A. Strong (2021). *StellarICS: Inverse Compton Emission from the Quiet Sun and Stars from keV to TeV*. arXiv: 2012.13126v2.

Peterson, L. E., D. A. Schwartz, and D. Pelling R. M. McKenzie (Dec. 1966). "The upper limit solar gamma-ray spectrum to 10 MeV". In: *Journal of Geophysical Research* 71.

Seckel, D., T. Stanev, and T. K. Gaisser (1991). "Signatures of cosmic-ray interactions on the solar surface". In: *The Astrophysical Journal* 382, pp. 652–666.

Siegert, Thomas (Apr. 2023). "The Positron Puzzle". In: *Astrophysics and Space Science* 368. DOI: 10.1007/s10509-023-04184-4.

Siegert, Thomas, Roland Diehl, Gerasim Khachatryan, Martin Krause, Fabrizia Guglielmetti, Jochen Greiner, Andrew Strong, and Xiaoling Zhang (Feb. 2016). "Gamma-ray spectroscopy of Positron Annihilation in the Milky Way". In: *Astronomy Astrophysics* 586. DOI: 10.1051/0004-6361/201527510.

Smerlack, M. (2010). "A Blackbody is Not a Blackbox". In: *European Journal of Physics* 32. DOI: 10.1088/0143-0807/32/5/002.

Smith, David, Robert Lin, Kevin Hurley, Wayne Coburn, Gordon Hurford, Claudia Wigger, Wojtek Hajdas, Alex Zehnder, Mark McConnell, and The Rhessi (Mar. 2003). "Nonsolar astronomy with the Reuven Ramaty High Energy Solar Spectroscopic Imager(RHESSI)". In: *Proceedings of SPIE - The International Society for Optical Engineering* 4851. DOI: 10.1117/12.461415.

Souami, D. and J. Souchay (July 2012). "The solar system's invariable plane". In: *Astronomy and Astrophysics* 543, pp. 133–. DOI: 10.1051/0004-6361/201219011.

Tie, S. S. (2015). *The Sun and its Iron Fist*. Accessed: 31.03.2024. URL: https://astrobites.org/2015/01/30/the-sun-and-its-iron-fist/.

Tomsick, John, Steven Boggs, Andreas Zoglauer, Dieter Hartmann, Marco Ajello, Eric Burns, Chris Fryer, Chris Karwin, C. Kierans, Alexander Lowell, Julien Malzac, Jarred Roberts, Pascal Saint-Hilaire, Albert Shih, Thomas Siegert, Clio Sleator, Toshiaki Taka-

hashi, Fabrizio Tavecchio, Eric Wulf, and Haocheng Zhang (Aug. 2023). *The Compton Spectrometer and Imager*.

Tomsick, John, Andreas Zoglauer, Clio Sleator, Hadar Lazar, Jacqueline Beechert, Steven Boggs, Jarred Roberts, Thomas Siegert, Alex Lowell, Eric Wulf, Eric Grove, Bernard Phlips, Terri Brandt, Alan Smale, C. Kierans, Eric Burns, Dieter Hartmann, Mark Leising, Marco Ajello, and Peter Ballmoos (Aug. 2019). *The Compton Spectrometer and Imager*.

Yu, Hongmei and Yan Guo (June 2024). "Survival Analysis". In: pp. 191–208. ISBN: 978-981-99-7389-7. DOI: 10.1007/978-981-99-7390-3_14.

Zoglauer, Andreas, R. Andritschke, and F. Schopper (Oct. 2006). "MEGAlib – The Medium Energy Gamma-ray Astronomy Library". In: *New Astronomy Reviews - NEW ASTRON REV* 50, pp. 629–632. DOI: 10.1016/j.newar.2006.06.049.

A. Appendix

A.1. Model programming and calculation of the significance

The following presents the key code, which was used for the evaluation of the models and the calculation of the significance.

```
    def lnprior(theta):     # flat prior
        a, b, c = theta
        return 0.0
    def lnlike(theta, x1, x2, y, erry):     # likelihood
        a, b, c = theta
        model = int_powerlaw(x1,x2,a,b) + int_gaussian(x1,x2,c)
        return -0.5*(np.sum( ((y-model)/erry)**2 ))
    def lnprob(theta, x1, x2, y, erry):     # The total posterior
        lp = lnprior(theta)
        if not np.isfinite(lp):
            return -np.inf
        return lp + lnlike(theta, x1, x2, y, erry)

    ndim, nwalkers = 3, 30
    pos = [result.x + 1e-4*np.random.randn(ndim) for i in range(nwalkers)]

    sampler = emcee.EnsembleSampler(nwalkers, ndim, lnprob, args=(E_min, E_max, F,
    ↪  error_y))

    from tqdm import tqdm_notebook as tqdm
    _ = sampler.run_mcmc(pos, 2000,progress=True)

    N_model = 2000
    y_models = np.zeros((N_model,samples_2.shape[0]))

    for i in range(samples_2.shape[0]):
        y_models[:,i] = powerlaw(x_data2,samples_2[i,0],amples_2[i,1]) +
        ↪  gaussian(x_data2,samples_2[i,2])

```

Listing 1: Creating of the power-law and gaussian model. 1σ of the upper limits from Peterson et al. (1966), Frost et al. (1966), and Hannah et al. (2007) were used as the input values for the error bar.

```
    def sign_2years_cont_position_calc(image,i,E_range,mw,exposure,sigma_wish=5):

    scale_factor = 1/u.day
    nominal_mission = 1*u.day

    cpy_bg = (BG_Flux[E_range]).to(1/u.day)

    counts_bg = cpy_bg*nominal_mission

    cpy_mw =
    ↪  np.sum(exposure[E_range]*mw*domega_sr*(MW_flux[E_range]/2.79e-03))*scale_factor

    counts_mw = cpy_mw*nominal_mission

    cpy_image = image[i][E_range]

    counts_image = cpy_image*nominal_mission

    image_signi_mw_bg = cpy_image / np.sqrt(cpy_image + cpy_mw + cpy_bg)

    sigma_wish = 5.
    signi_wish = (sigma_wish/image_signi_mw_bg)**2 * u.day

    sign_cont_2years_position.append(image_signi_mw_bg)

```

Listing 2: Calculation for the significance of a source within one day and for different energy ranges. 730 different sources at different positions were used to obtain the significance for 2 yr from the "moving" Sun.

A.2. Simulation for the astrophysical model

```
# Global parameters
Version         1
Geometry        /Users/linusstricker/Downloads/massmodel-cosi-smex-v12/COSISMEX.geo.setup

# Physics list
PhysicsListEM               LivermorePol

# Output formats
StoreSimulationInfo         all

# Run & source parameters

Run SpaceSim
SpaceSim.FileName           Sun_peterson_1
SpaceSim.Time               1835573699.0
SpaceSim.OrientationSky     Galactic File NoLoop /Users/linusstricker/Orientation_days/
orientation_day_1.txt

SpaceSim.Source Sun1
Sun1.ParticleType           1
Sun1.Beam                   FarFieldPointSource 0 0
Sun1.Orientation            Galactic Fixed -59.51787602025056 109.65493443840994
Sun1.Spectrum               BrokenPowerLaw 150 5000 1273.01 1.973 1.302
Sun1.Flux                   4.681276e-5
Sun1.FarFieldTransmissionProbability /Users/linusstricker/Downloads/
TP_Earth_occultation_550km_zenith_pointing.dat
```

Figure A.1.: Source file for one day with the Sun at the the position $(\ell, b) = (110°, -60°)$.

```
Event selections:

All events  ..................... 208074
Not rejected events  ........... 72924

Rejection reasons:

Not good  ......................  16292
Event Id .......................  0
Detector of 1st interaction ....  0
Detector of 2nd interaction ....  0
Beam selection .................  0
Box selection  .................  0
Total energy  ..................  0
Time  ..........................  0
Time walk  .....................  0
Electron energy  ...............  0
Gamma energy  ..................  0
Compton angle  .................  0
First Lever arm  ...............  1306
Any lever arm  .................  0
Length Compton sequence ........  0
Clustering quality factor ......  0
Compton quality factor .........  0
Track quality factor ...........  0
Coincidence window .............  0
Earth-Horizon cut ..............  0
Pointing .......................  0
Max. theta deviation ...........  0
Max. ARM .......................  0
Max. SPD .......................  0
Length track ...................  0
Opening angle pair  ............  0
Initial energy deposit pair  ...  0
Pair quality factor ............  0
Use photos  ....................  117646
Use pairs  .....................  0
Use Compton  ...................  0
Use tracked Compton  ...........  0
Use not tracked Compton  .......  0
Use muons  .....................  0
Use PET  .......................  0
Use multi  .....................  0
Use unidentifiables  ...........  11202
Use decays  ....................  0
Use flagged as bad  ............  11202

ACCEPTED  ......................  72924
ANALYZED  ......................  208074
```

Figure A.2.: Output for the event selection after the simulations with `Mimrec`[1].

Eidesstattliche Erklärung

Hiermit erkläre ich, dass ich die vorliegende Arbeit eigenständig und ohne fremde Hilfe angefertigt habe. Textpassagen, die wörtlich oder dem Sinn nach auf Publikationen oder Vorträgen anderer Autoren beruhen, sind als solche kenntlich gemacht. Die Arbeit wurde bisher keiner anderen Prüfungsbehörde vorgelegt und auch noch nicht veröffentlicht.

Würzburg, 19.08.2024

Linus Stricker